Master Thesis

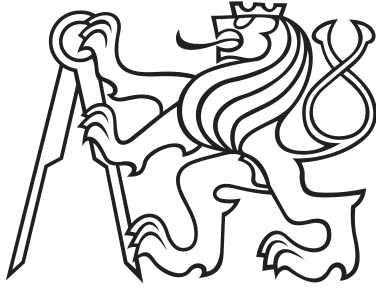**Czech Technical University in Prague**

F2

Faculty of Mechanical Engineering
Department of Aerospace Engineering

Aircraft Propulsion with Static Recuperation

Bc. Ondřej Šantora

Supervisor: Ing. Jan Klesa, Ph.D.
Field of study: Aerospace Engineering
January 2021

ZADÁNÍ DIPLOMOVÉ PRÁCE

I. OSOBNÍ A STUDIJNÍ ÚDAJE

Příjmení: **Šantora**　　Jméno: **Ondřej**　　Osobní číslo: **482636**

Fakulta/ústav: **Fakulta strojní**

Zadávající katedra/ústav: **Ústav letadlové techniky**

Studijní program: **Letectví a kosmonautika**

Studijní obor: **Letadlová a kosmická technika**

II. ÚDAJE K DIPLOMOVÉ PRÁCI

Název diplomové práce:

Pohon letadla se statickou rekuperací

Název diplomové práce anglicky:

Aircraft Propulsion with Static Recuperation

Pokyny pro vypracování:

Pro vypracování proveďte:
- Rešerše pohonných systémů letadel
- Návrh pohonného systému
- Výpočet proudění ve vstupním ústrojí metodou CFD
- Analýza výsledků
- Návrh modifikací pro zvýšení výkonů
- Porovnání se standardním pohonným systémem

Seznam doporučené literatury:

Dle pokynů vedoucího práce

Jméno a pracoviště vedoucí(ho) diplomové práce:

Ing. Jan Klesa, Ph.D.,　ústav letadlové techniky　FS

Jméno a pracoviště druhé(ho) vedoucí(ho) nebo konzultanta(ky) diplomové práce:

Datum zadání diplomové práce: **30.10.2020**　　Termín odevzdání diplomové práce: **15.01.2021**

Platnost zadání diplomové práce: ＿＿＿＿＿＿＿＿

＿＿＿＿＿＿＿＿＿＿＿＿＿＿＿＿
Ing. Jan Klesa, Ph.D.
podpis vedoucí(ho) práce

＿＿＿＿＿＿＿＿＿＿＿＿＿＿＿＿
Ing. Robert Theiner, Ph.D.
podpis vedoucí(ho) ústavu/katedry

＿＿＿＿＿＿＿＿＿＿＿＿＿＿＿＿
prof. Ing. Michael Valášek, DrSc.
podpis děkana(ky)

III. PŘEVZETÍ ZADÁNÍ

Diplomant bere na vědomí, že je povinen vypracovat diplomovou práci samostatně, bez cizí pomoci, s výjimkou poskytnutých konzultací.
Seznam použité literatury, jiných pramenů a jmen konzultantů je třeba uvést v diplomové práci.

＿＿＿＿＿＿＿＿＿＿＿＿＿＿＿＿
.
Datum převzetí zadání

＿＿＿＿＿＿＿＿＿＿＿＿＿＿＿＿
Podpis studenta

Acknowledgements

Declaration

I hereby declare that the present diploma thesis was composed by myself and that the work contained herein is my own. I also confirm that I have only used the specified resources. All formulations and concepts taken verbatim or in substance from printed or unprinted material or from the Internet have been cited according to the rules of good scientific practice and indicated by footnotes or other exact references to the original source.

The present thesis has not been submitted to another university for the award of an academic degree in this form. This thesis has been submitted in printed and electronic form. I hereby confirm that the content of the digital version is the same as in the printed version.

I understand that the provision of incorrect information may have legal consequences.

Abstract

This thesis studies the possibilities of improving aircraft propulsion system efficiency by engaging the concept of static recuperation. The idea is to improve overall thrust by aerodynamic forces acting on static blades placed in the propulsion system's intake.

Firstly, the history of aircraft propulsion is briefly described. Subsequently, the most common aircraft propulsion systems are introduced with a focus on their fuel consumption. The promising hybrid and all electric propulsion systems are also elaborated. The chapter *Theory of recuperative propulsion* deals firstly with different physical models that are used to describe aerospace propulsion with different levels of fidelity. This chapter also provides the theoretical background for the recuperation model.

Based on the findings of previous chapters, a 3D model of a recuperative propulsion is designed using *NX Siemens* CAD software. This model is intended as a test unit and is built around real components (mainly the HET 9305 impeller) and can be used later on for a real lab testing. Finally, a CFD simulation of this propulsion system was performed using *Ansys Fluent* software. The simulation results show that this concept could be advantageous particularly for lower flight speeds where the static blades are able to provide significant additional thrust.

Keywords: Aircraft Propulsion, Recuperation, CFD, Thermodynamics, Electric Aircraft Propulsion, ZetJet

Supervisor: Ing. Jan Klesa, Ph.D.

Abstrakt

Tato práce se zabývá možnostmi, jak vylepšit účinnost leteckého pohonu použitím konceptu statické rekuperace. Myšlenkou tohoto konceptu je využít aerodynamické síly působící na statické lopatky ve vstupním ústrojí ke zvýšení celkového tahu systému.

Nejdříve je stručně popsána historie pohonu letadel. Následně jsou představeny nejčastěji používané letecké pohony a je také probrána jejich účinnost. Zmíněny jsou i nadějné pohonné systémy budoucnosti, jako třeba hybridní pohonné systémy a čistě elektrické pohonné systémy. V kapitole o teorii jsou představeny fyzikální modely, které jsou v současnosti používány k teoretickému popisu pohonu letadel, přičemž je diskutována jejich míra korespondence s realitou. V této kapitole je také probrána teorie stojící za konceptem statické rekuperace, jak je v této práci chápána.

Na základě poznatků z předcházejících kapitol je poté vytvořen 3D model pomocí CAD programu *NX Siemens*. Tento model je zamýšlen jako testovací jednotka tohoto systému a je postaven okolo reálného dmychadla HET 9305, pro případné snazší vyrobení a testování prototypu. Nakonec je provedena CFD analýza systému s použitím výpočetního software *Ansys Fluent*. Výsledky simulace ukazují, že tento systém může být použitelný, a to zejména pro nižší rychlosti letu, kde jsou statické lopatky schopny poskytnout přídavný tah do systému.

Klíčová slova: pohon letadel, rekuperace, CFD, termodynamika, elektrický pohon letadel, ZetJet

Překlad názvu: Pohon letadla se statickou rekuperací

Contents

Figures

Tables

Chapter 1

Introduction

1.1 History of the Pursuit of Aircraft Fuel Efficiency

Since people have started building and using airplanes as means of transport, there was a need to decrease fuel consumption as much as possible. Especially during the post-war upswing of commercial air transport in the 1960s and 1970s, there was a great leap in aircraft efficiency, driven mostly by an effort to save on fuel. However, fuel costs alone have not been sufficient to stimulate increased aircraft efficiency, and improvements in fuel efficiency due to the introduction of new aircraft have decreased over time. These findings suggest that a CO_2 standard that applies to newly built aircraft has also had a significant impact on emissions reduction in previous decades. [1]

As we can see on modern airliners, the basic aerodynamic design has remained almost unchanged since the beginning of the jet era. Let's look at one of the most iconic passenger aircraft of all times, the Boeing 747 Jumbo Jet. While the shape of the still produced aircraft has remained almost unchanged since its roll out more than half a century ago, the engines have come a long way to higher fuel efficiency. While there is still ongoing aerodynamic optimization of wings and fuselage, the aforementioned increase of fuel efficiency was mostly caused by the massive enhancement of the airplane engines. As shown in Table 1.1, the bypass ratio (BPR) of modern aircraft engines can be more than five times higher than in the 1960s. The bypass ratio is the mass flow rate of air going only through
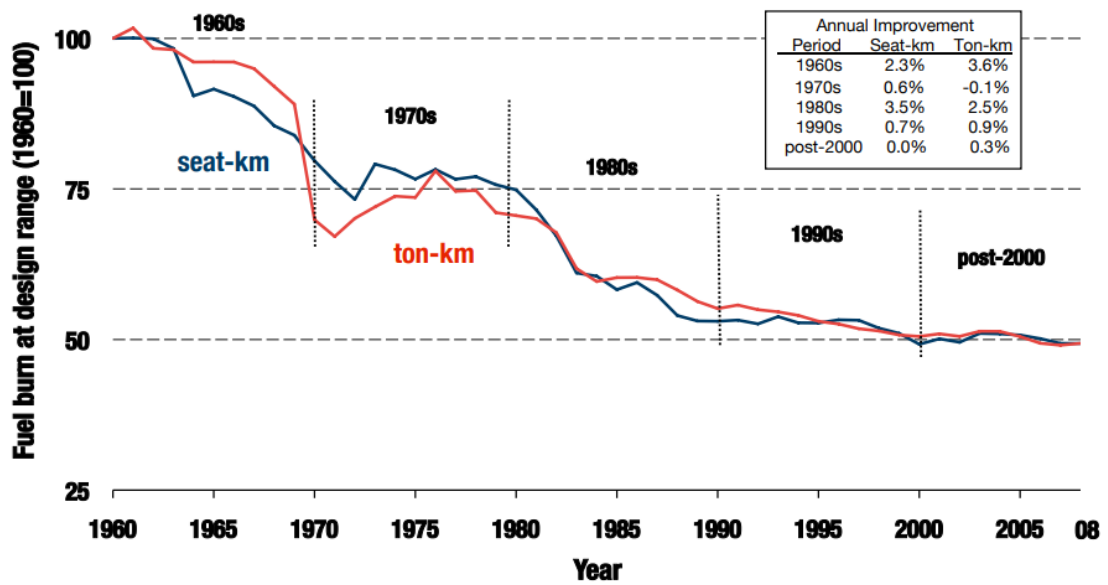
Figure 1.1: Progress of commercial aircraft fuel consumption per seat and per tonne [1]

the fan at the engine inlet, divided by the mass flow rate of air going through the turbomachinery in the engine core. The principle of BPR increasing fuel efficiency of the engine will be discussed later on in this chapter.

Aircraft	Year	Engine	BPR
B747-100	1968	Pratt & Whitney JT9D	4.80
B747-800	2011	General Electric GEnx	9.00
B737-100	1967	Pratt & Whitney JT8D	1.74
B737-MAX	2016	CFM LEAP-1B	9.00

Table 1.1: Comparison of bypass ratio in 1960s vs. now. [2, 3, 4, 5]

1.2 Future of Civil Aviation in Fuel-Efficiency Prospective

According to the International Air Transport Association's (IATA) report [6], the volume of air transport has doubled every fifteen to twenty years since the 1950s. Even with the previously mentioned efforts to lower fuel consumption, it is obvious

that air transport's negative impact on the environment is increasing every year. The report also states that all aviation stakeholders have agreed, among other things, on reducing global net carbon emissions by 50 % by 2050 relative to 2005. By 2030, IATA expects fuel efficiency improvement by approximately 25 % by
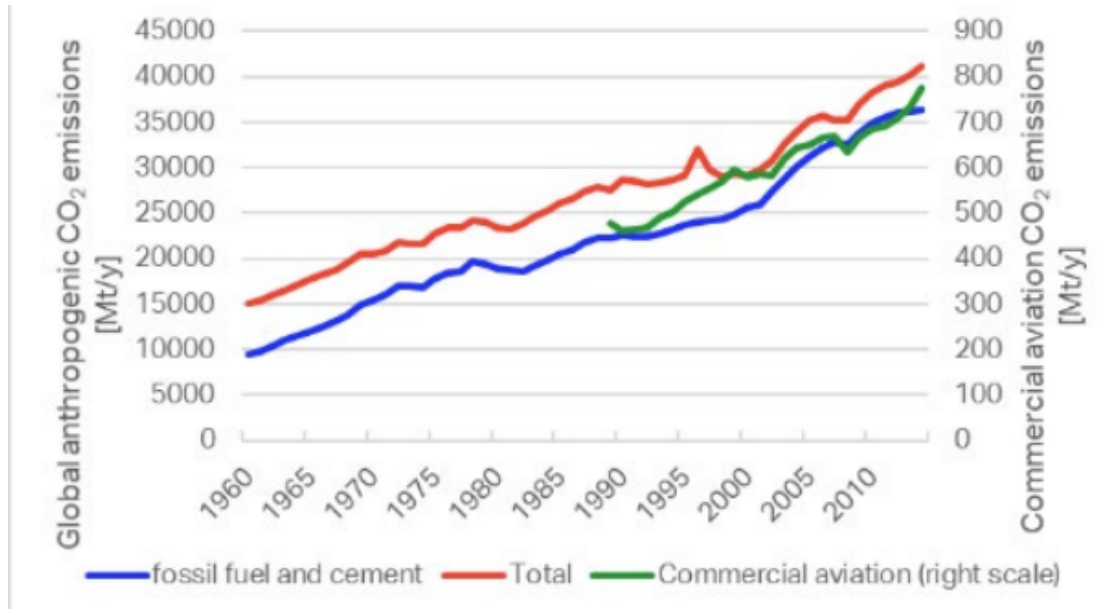
Figure 1.2: Commercial aviation CO_2 emissions compared to all anthropogenic emissions [6]

enhancing existing turbofan technology. Then, by 2035, Hybrid-Electric Aircraft design is expected, potentially improving fuel efficiency by 40 %. By 2040, usage of fully electric aircraft is predicted which for carbon-neutral energy sources means also zero emissions from aircraft operation. While in most countries we cannot expect all electricity to be carbon neutral by that time which means we still should continue to pursue as effective aircraft and their propulsion systems as possible, both for decreasing emissions and for elongating range which is going to be the single most challenging issue in electric flight due to the lower energy density of batteries compared to kerosene.

Since the dawn of Civil Aviation, classical aircraft design has consisted of a fuselage, wings with attached jet engines, and vertical and horizontal stabilizers. This may change in upcoming decades since almost all aircraft manufacturers and aerospace research centers keep developing new aircraft concepts that disrupt these traditions. Even though these concepts use advanced turbofans, it is obvious that prospectively

there will also be a demand for new efficient propulsion systems like the one being studied in this thesis. One of the disruptive aircraft designs is a result of a joint venture between KLM Royal Dutch Airlines, Delft University of Technology, and Airbus. The scale model of their concept *Flying V* successfully flew for the first time. [7] Another example of blended wing aircraft is from a joint venture between Boeing, NASA, and Cranfield University. [8] One of the famous American X-planes, called X-48 has also successfully finished many test flights.

(a) : Flying V [7]

(b) : Boeing X-48 [8]

Figure 1.3: Blended wing aircraft concepts

Aviation's transformation towards carbon neutrality will demand a lot of effort and funding. Only the EU, in its Clean Aviation report [9] has committed to invest €12 billion in Research & Innovation. This is expected to lead to €50 billion in Product Development and finally to €5000 bn. in Product Deployment. Therefore, *now* is the right time to develop new ideas in aerospace propulsion systems.

Chapter 2

Review of Existing Aircraft Propulsion Systems

This chapter briefly explains the theoretical background of gas-turbine propulsion and then presents some of the most common propulsion systems.

2.1 Theory of Propulsion

Generally, every existing propulsion system can be described by using Newton's Second Law, or conservation of momentum. For an isolated system, it states that the time rate change of momentum equals force, in the mathematical form [10], for a vehicle of mass m traveling with velocity V:

$$m\frac{dV}{dt} = F \tag{2.1}$$

Now we can use the same principle for a propulsion device with inlet velocity V_{in} and outlet velocity V_{out}. The mass flow rate through this device is $\dot{m}$. Then we can write this simplified relationship for the device's thrust force F:

$$\dot{m}(V_{out} - V_{in}) = F \tag{2.2}$$

This equation is of course usable only for low fidelity models, as it omits the pressure forces effects at the inlet and outlet. Taking into consideration also the pressure forces acting on the control volume (CV) and time rate of change of momentum inside CV, we can summarize the conservation of momentum in the direction of

the thrust force F [10]:

$$\frac{d(mV)_{CV}}{dt} = \dot{m}_{in}V_{in} - \dot{m}_{out}V_{out} + F + (p_a - p_e)A_e \tag{2.3}$$

where subscript a stands for ambient, e for exit, and m and V are the properties of the air in the CV. For many purposes, we only want to deal with the engine in steady flight which means the left side of 2.3 equals zero. Also, after introducing the fuel-air ratio $f = \dot{m}_{fuel}/\dot{m}_{air}$, the force equation is:

$$F = \dot{m}_{in}[(1 + f)V_{out} - V_{in}] + (p_e - p_{in})A_e \tag{2.4}$$

This also applies to electric propulsion systems, where $f = 0$ as no physical mass is burned. Thus, we can say that the objective of any propulsion system is to obtain excess momentum at the outlet, usually by generating high-speed exhaust jets. Nowadays, the energy needed for momentum increase is usually obtained by burning kerosene, however, more and more recently designed concepts use electrical power either from batteries or from solar panels. This thesis will also discuss harvesting energy from the atmosphere surrounding the aircraft. In air-breathing engines, the vast majority of exhaust jets are molecules of air, with just a minor proportion being combustion byproducts. For rocket motors operating outside the atmosphere, the exhaust consists solely of combustion products but these propulsion systems aren't the subject of this thesis. For reference see [10, 11, 12].

2.2 Gas-Turbine Engines

Gas-turbine propulsion systems are the most common in this day and age. Kerosene is used as fuel, having a *Lower Caloric Value* (LCV) of 43.1 MJ/kg. Ideal cycles are used for low-fidelity models during engine research and development. The Brayton Cycle is usually used to describe the thermodynamics processes in a Gas-Turbine engine [10]. This cycle simplifies all processes in an engine into four steps taking place in four engine components:

1. COMPRESSOR: isentropic compression of air through the compressor

2. COMBUSTOR: isobaric heat addition

3. TURBINE: isentropic expansion generating shaft power

4. NOZZLE: isentropic acceleration into ambient conditions

In Figure 2.2, the compressor is between points 1 and 2, the combustor between points 2 and 3, both the turbine and nozzle are between 3 and 4. For open cycles as Gas-Turbine engine there is no connection between points 4 and 1 in diagrams 2.2.
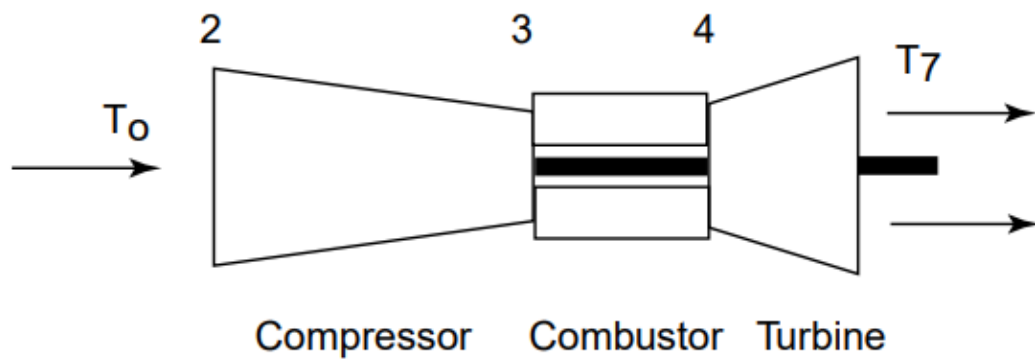
Figure 2.1: Basic layout of a Gas-Turbine Engine used for Brayton Cycle model [10]
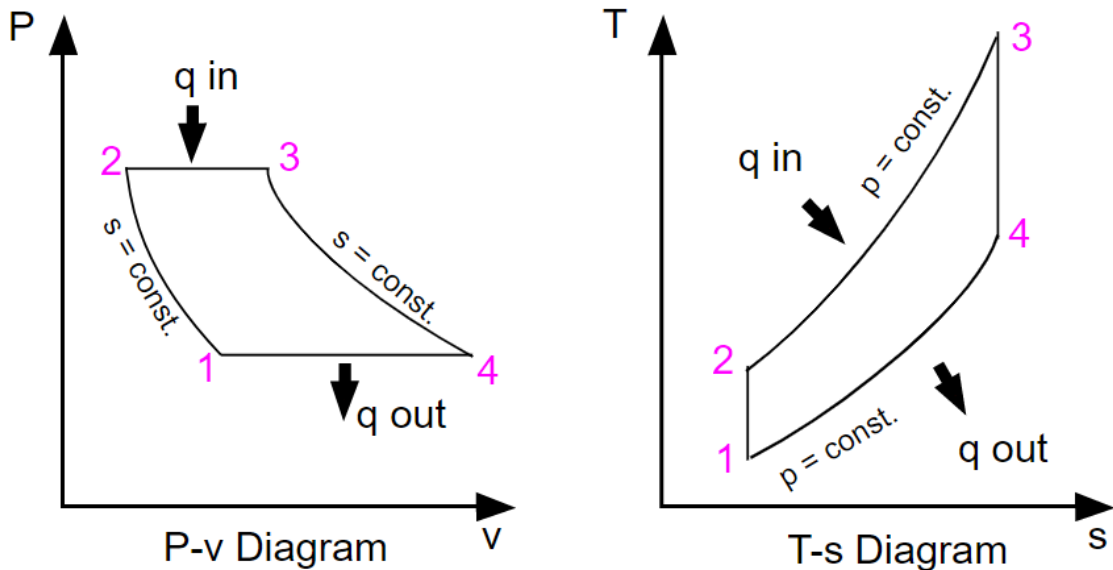
Figure 2.2: Ideal Brayton Cycle in p-v and T-s diagrams [13]

The reason for using the ideal cycles is to obtain thermal efficiency η_T, defined as clear *power output* divided by *heat input rate*. It's simply the efficiency the

engine would have if all processes were ideal as described above and if there were no rolling resistances in rotating parts and no frictions overall.

$$\eta_T = \frac{\dot{W}_{out} - \dot{W}_{in}}{\dot{Q}_{in}} \tag{2.5}$$

where $\dot{W}_{out}$ stands for work rate (or power) generated by the turbine and $\dot{W}_{in}$ is the power consumed by the compressor - which is why it has a minus sign in accordance with the convention for power converted from machinery to gas. After modification of equation 2.5 thermal efficiency can be obtained as a function of total temperature or total pressure. The total (sometimes called stagnation) quantities (pressure, temperature...) are the properties a gas flow would have if brought to rest adiabatically, meaning that all of the flow's kinetic energy has been converted to internal energy.

$$\eta_T = 1 - \frac{T_0}{T_3^0} = 1 - \frac{1}{\left(\frac{p_3^0}{p_0}\right)^{\frac{\gamma-1}{\gamma}}} \tag{2.6}$$

Quantities with subscript 0 are ambient, quantities with subscript 3 are in the flow after the compressor and before the combustion chamber. γ is the *Heat capacity ratio* defined as the ratio of isobaric heat capacity c_P and isochoric heat capacity c_V. The denominator of the expression on the right-hand-side in 2.6 is called *overall pressure ratio* and it is the only variable the thermal efficiency depends on, thus we can plot *Thermal efficiency* as a function of *Pressure ratio*.
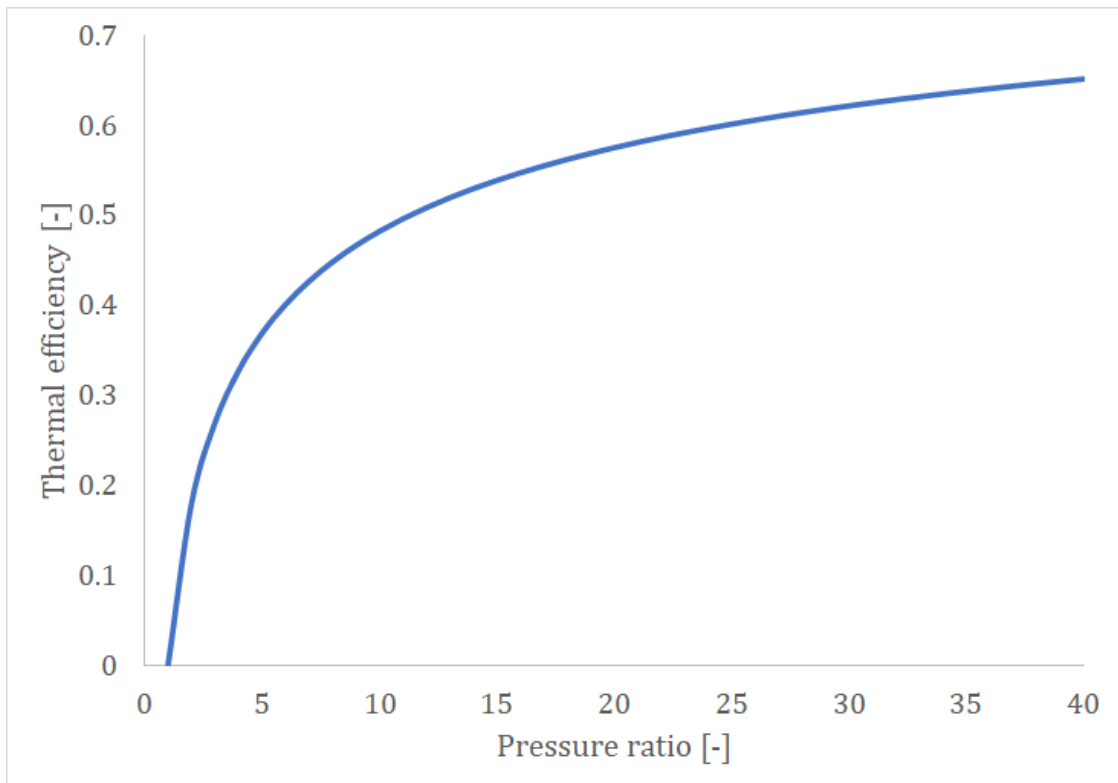
Figure 2.3: Thermal efficiency as a function of Pressure ratio [10]

As shown in Figure 2.3, the efficiency becomes propitious when the compression ratio is equal to at least 10 to 15. The temperature ratio in Equation 2.6 also shows that thermal efficiency of 1.0 can only be reached if the temperature in the engine's combustion chamber increased without bound. As real materials can only withstand finite temperatures, the absolute thermal efficiency cannot be reached. The shape of the curve in Figure 2.3 only applies to an ideal cycle, a local maximum usually appears on this kind of curve for a real cycle.

2.2.1 Turboprop Engine

The turboprop is a type of Gas-Turbine engine which produces most of its thrust using a shaft-driven propeller. A certain portion of the thrust, however, is also produced employing a hot-exhaust jet. The shaft is driven by a turbine of much smaller diameter and at higher RPM. Hence, the propeller requires a speed reduction unit of a ratio of about 15:1 to reduce stresses from centrifugal forces acting on the propeller [12]. Another consequence of large diameter propellers is a high Mach

number at the propeller's blades. Trans-sonic effects at propeller tips decrease its efficiency and make turboprops unviable above approx. Mach 0.7 [11]. Turboprops are also noisier and heavier than turbojets of similar power. Nevertheless, the noise and the aforementioned stresses from centrifugal forces can be reduced by utilizing more of the smaller blades. Advanced turboprops use variable pitch blades enabling higher efficiencies in a wide operating range of flight speeds [11]. Turboprops are more efficient for lower flight speeds as they accelerate a larger volume of air by smaller magnitude in comparison with turbojets or turbofans. For this reason, they are still used for slower and smaller passenger aircraft.
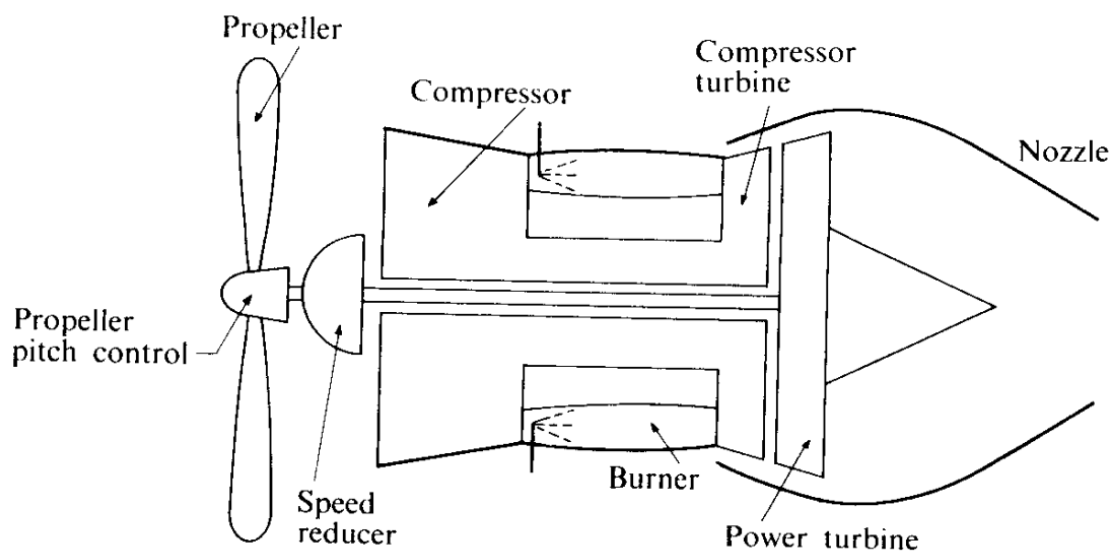
Figure 2.4: Schematic diagram of the turboprop engine [12]

The thermodynamics cycles of the engine and its efficiencies were quantified in Section 2.2. The thrust of the propeller itself is examined next.
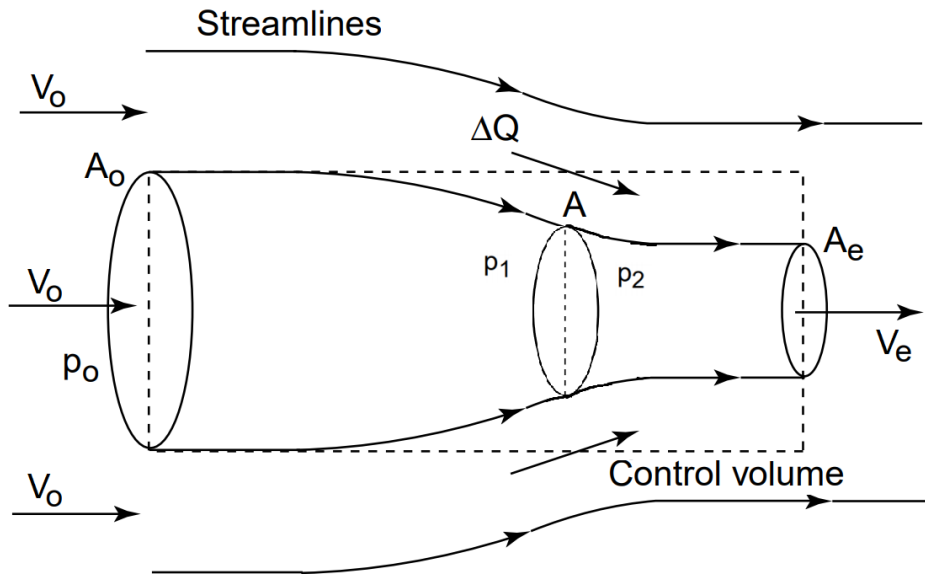
Figure 2.5: Control volume analysis for propeller thrust [10]

A basic control volume model is used to determine a propeller's thrust in Figure 2.5. Air density is considered constant ($\rho = const.$) and ΔQ stands for volumetric flow rate $[m^3/sec]$ entering the control volume at the propeller. The control volume is bordered by the dashed line. There's a free stream with quantities subscribed 0 on the left-hand side. The propeller then accelerates the flow making the stream tube narrower. On the right-hand side, the air in the stream tube has velocity U_e and the air in the CV but out of the stream tube has still velocity U_0. With these assumptions we can express the overall volume-flow rate [10]:

$$A_0 U_0 + \Delta Q = A_e U_e + (A_0 - A_e)U_0 \tag{2.7}$$

Then, thrust can be calculated using the momentum equation with mass flow rates and velocities. Using quantities from Figure 2.5 and Equation 2.7, thrust expression can be adjusted [10]:

$$F = \dot{m}_{out} V_{out} - \dot{m}_{in} V_{in} = \rho[A_e V_e^2 + (A_0 - A_e)V_0^2] - \rho A_0 V_0^2 - \rho \Delta Q V_0 \tag{2.8}$$

After solving Equation 2.7 for ΔQ and inserting into Equation 2.8 we can obtain a simpler relationship for thrust [10]. This can be also expressed using mass flow rate

11

$\dot{m}$ in [kg/s]:

$$F = \dot{m}_e(V_e - V_0) \tag{2.9}$$

2.2.2 Turbojet Engine

Another type of Gas-Turbine engine is a turbojet. Its efficiency is disadvantageous for low flight speeds [14] which is why they have been replaced by more efficient turbofans for most transport aircraft. Nevertheless, they remain a useful alternative for cruise missiles or supersonic applications. For example, the well-known supersonic airliner *Concorde* was propelled by four of Rolls-Royce Olympus 593 turbojets which enabled it to travel at flight speeds up to Mach 2 [14].
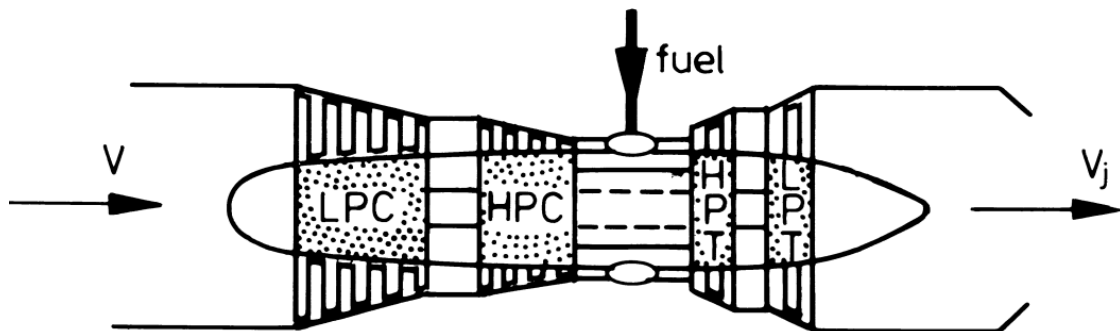
Figure 2.6: Concorde's propulsion unit: turbojet Rolls-Royce Olympus 593 [14]

The turbojets usually have more so-called spools, which is a compressor and a turbine mounted on one shaft. There's a turbojet with two spools, low pressure (LP) and high pressure (HP) in Figure 2.6. This design with more spools increases the turbojet's performance at the start and lower flight speeds. Because the temperature of the hot gas entering the turbine must be maintained far below the adiabatic combustion temperature due to temperature limits of turbine material, there's still a lot of oxygen for a secondary combustion after the turbine [12]. From a thermodynamics point of view, an afterburner is fuel inefficient but is advantageous during take-off, transsonic speeds, and shorter supersonic sprints especially in combat applications. To obtain maximum thrust from the engine in both afterburning and non-afterburning operation, an adjustable exhaust nozzle is necessary [15].

2.2.3 Turbofan Engine

As discussed earlier, the turbofan evolved from the turbojet in order to increase its efficiency [14]. It contains all parts that the turbojet has, and additionally to that. it also has the fan, driven by a shaft connected to a turbine. Part of the airstream from the fan feeds into the engine's core, which is simply a turbojet, and the rest of the air bypasses the core, flowing between the core's coating and the engine's outer nacelle. Turbofans can be divided into low-bypass and high-bypass using the ratio of the mass flow rate through core and bypass streams. Low-bypass turbojets were used to propel earlier jet airliners and are still used for military aircraft, often with an afterburner. High-bypass turbofans are used for modern airliners, sometimes having the BPR even higher than 10 [16].
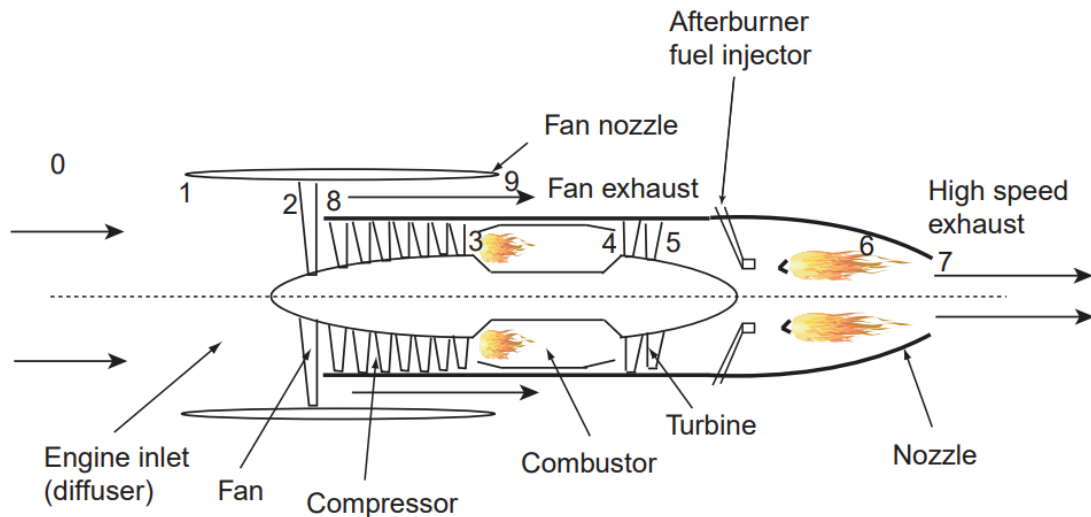
Figure 2.7: Schematic view of a turbofan with an afterburner [10]

Bypass ratio (BPR) is denoted α and it's a ratio of the mass flow rate through bypass and core:

$$\alpha = \frac{\dot{m}_{bypass}}{\dot{m}_C} \tag{2.10}$$

Using the same basic relationships of Newtonian mechanics and the station numbering from Figure 2.7 we can express the thrust of ideal turbofan as a function

13

of local velocities and mass-flow rates [10]:

$$F = \dot{m}_C(V_7 - V_0) + \dot{m}_{bypass}(V_9 - V_0) \tag{2.11}$$

2.3 Hybrid Propulsion Systems

Hybrid propulsion systems use two or more energy sources to propel a vehicle. Hybrid systems are widespread and have a long history in railroad locomotives. Lately, they also experience a great boom in automotive. The main reason for the use of hybrid systems is the optimization of fuel consumption, by storing energy that would otherwise be lost, usually in batteries, and then using it to supplement vehicle propulsion later [17]. While there are multiple possible configurations used in hybrid systems, usually they consist of a combustion engine and an electric motor.

2.3.1 Serial Hybrid Propulsion

This type of hybrid propulsion system lacks direct mechanical interconnection between the combustion engine and propeller [18]. This means that the combustion engine drives the generator to produce electricity which is then used to drive an electric motor that drives directly the propeller. Usually, there is also a battery in the system to store excess energy. There are still many possibilities of how serial configuration can be arranged, one of which is depicted in Figure 2.8.
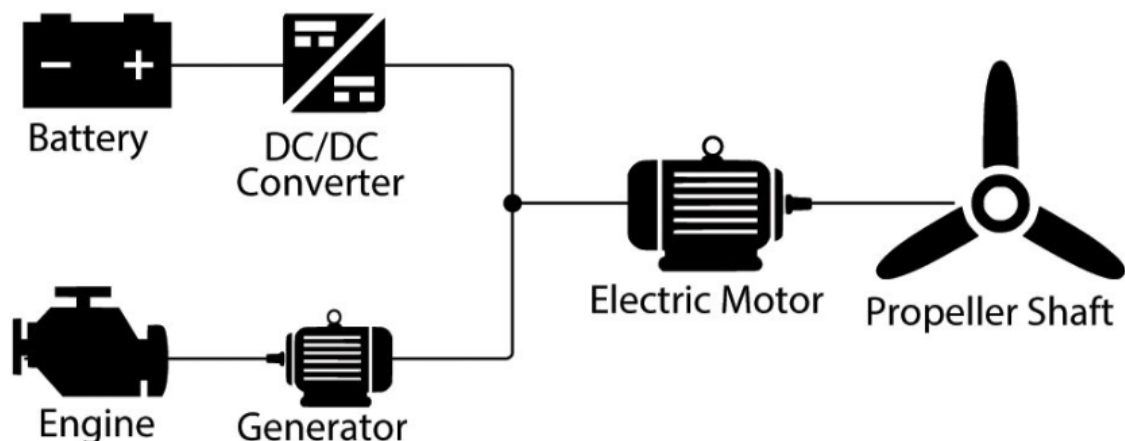
Figure 2.8: Serial hybrid propulsion system's scheme. [19]

Since the energy in this configuration is transmitted by wires, the designer has the freedom to place its components favorably with respect to the aircraft's mass distribution. Also, the combustion engine can be tuned to the most advantageous operation conditions (particularly RPM), which allows to fine-tune its efficiency. Unfortunately, there's no redundancy in the case of electric motor failure [18].

2.3.2   Parallel Hybrid Propulsion

Aircraft's propeller in this configuration is mechanically connected to the electric motor, as well as to the combustion engine. The parallel systems can operate on three regimes: running purely on the electric motor, purely on combustion, or combining both of them [17]. As usual, there are also batteries to store energy and provide it when needed, like during take-off.
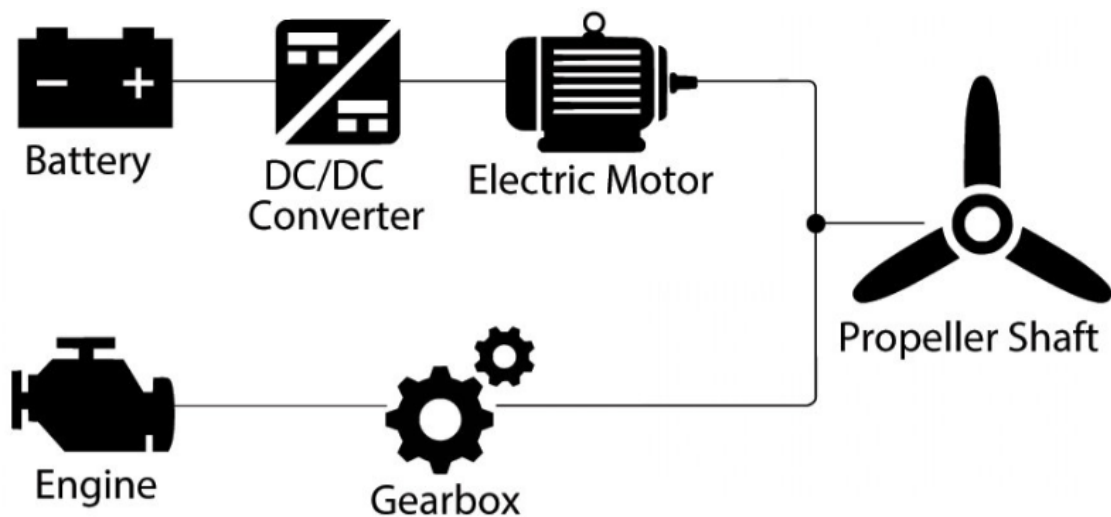
Figure 2.9: Parallel hybrid propulsion system's scheme. [19]

This configuration provides the advantage of redundancy in case of failure of one of the subsystems. Also, thanks to short boosts by an electric motor, there's not a necessity to accommodate more powerful and heavy combustion engines. On the other hand, all system components need to be installed nearby, as they're mechanically linked [18].

2.4 Electric Propulsion Systems

Electric propulsion has the potential to eliminate many of the Gas-Turbine (GT) engine's drawbacks, like high noise level, greenhouse gas emissions, low efficiency, or high maintenance requirements. An obvious disadvantage limiting their wider employment is the low power density of batteries [20]. Let's look at electric propulsion's benefits and challenges in comparison with GT engines according to [21]:

Benefits

- Efficiency about 96 %, which is 20 % higher than advanced turbofans

- No power lapse with altitude

- Compact engine

- Reliable

- 15dB lower noise level than GT

Challenges

- Energy density of Li-Ion batteries 0.8 MJ/kg compared to Jet Fuel's 44 MJ/kg

- Longer battery charging times

- Battery aging

- High-voltage transmission/distribution issues

- Thermal management

- Uncertainty of cost

There are two basic types of electric motors:

AC Motors

The most common AC Motor is an **asynchronous** (also called induction) motor. The electric current which produces a force (more precisely torque) in the rotor comes from the magnetic field of the stator made usually from copper winding. Since the stator is connected to alternating current, the magnetic field it produces changes periodically, causing the rotation of the rotor. The motor is characterized by slip, which is the difference between the angular velocity of the rotary magnetic field and the angular velocity of the rotor. The slip is necessary to induce a current in the rotor winding.

Another widely used AC motor is a **synchronous** motor. Here the rotor's angular velocity equals the angular velocity of the magnetic field produced by the stator. Above a certain size, synchronous motors are not self-starting, therefore they need some supplemental mechanism to initiate rotation. When connected to excessive load, the parts of the motor can lose its synchronization, resulting in the stopping of the motor. Thanks to their precise rotating speeds, smaller synchronous motors are widely used in analog clocks and other appliances where precision is required. Alternating current motors have a relatively high power capability and are cheaper compared to DC, but are cumbersome to control.

DC Motors

Direct current motors produce less rotor heat, have a wide spectrum of optimal power settings, and lose no energy due to the DC/AC conversion. Even though the DC motors are more expensive, especially because of the permanent magnets, they are more common due to their optimal power setting variability [20].

All electric motors need a variable magnetic field to operate. The alternating current itself provides the variability in the case of AC motors. For DC motors, this issue was originally solved by brushes connected to a rotating commutator, which changed the polarity of the current powering the coils in the stator. This layout is characterized by many drawbacks resulting from the mechanical friction of brushes and commutator, like the wear of moving parts and thus increased maintenance demand, power loss on brushes, possibly dangerous spark generation, or increased noise level.

These drawbacks are eliminated by the *Brushless DC motors* (**BLDC**) which

17

makes them ideal candidates for electric aircraft propulsion [22]. There are many promising aircraft propulsion projects based on BLDC motors, for instance, the SP200D electric motor developed by Siemens in cooperation with Rolls-Royce, Airbus, and others [23]. This world-setting motor delivers a power output of 260 kilowatts with a weight of just 50 kg, which means it reaches an impressing power-to-weight ratio over 5 kW/kg. The usual layout of the BLDC motor consists of a stator with coils and an outer rotor with permanent magnets. This kind of electric motor was limited by control technology until recently, but now the controllers are able to work reliably and power the coils in the way that the rotor still "chases" their magnetic field. This of course requires fast and precise measurement of the rotor's position, which is usually executed by a sensor based on the Hall Effect (the effect of getting a measurable voltage when a conductor or semiconductor with current flowing in one direction is introduced perpendicular to a magnetic field).
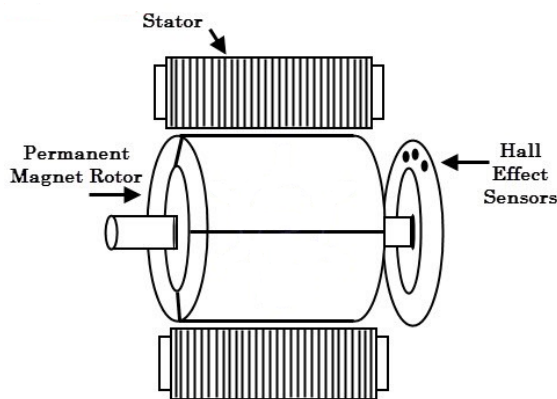
Figure 2.10: Brushless DC motor (BLDC). [24]

Batteries are not the only potential energy source for electric aircraft. There are many others, let's mention at least the most promising ones:

■ Solar Cells

Solar cells (SC) convert sunlight into electrical energy. Their typical efficiency usually doesn't get over 30 % in real conditions, consequently, a large area of SC is needed to provide sufficient power [20]. Since their performance is weather and day/night dependent, they are not applicable as a primary energy source but can be effective as a complement to batteries.

◼ Fuel Cells

Fuel cells (FC) are a source of electrical energy somewhat similar to batteries. Both use chemical reactions to generate electricity instead of using moving parts. However, batteries just store energy, fuel cells produce it continuously as long as a fuel and oxidant are supplied [20]. Hydrogen can be made on-board by chemical reactions or stored as high-pressure gas, which may cause safety issues.
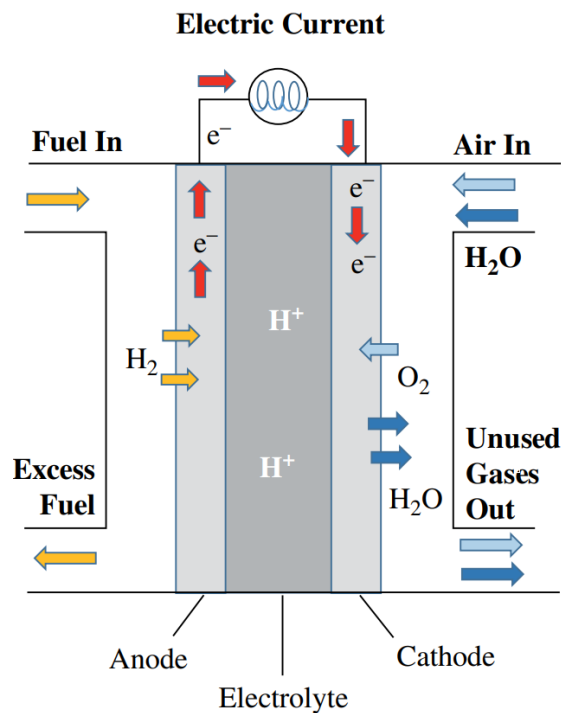
Figure 2.11: Fuel cell scheme. [21]

Fuel cells have many advantages, for example producing only heat and water as byproducts or theoretically unlimited scalability. On the other hand, there are still many issues with storage, durability, and costs [20]. FCs already have quite a long flight heritage as low power energy sources, for example onboard some manned spacecraft since the Gemini program [21]. FCs are classified based on their electrolyte solution:

- ◼ Alkaline Fuel Cell (AFC)

- ◼ Molten Carbonate Fuel Cell (MCFC)

- ◼ Phosphoric Acid Fuel Cell (PAFC)

■ Proton Exchange Membrane Fuel Cell (PEMFC)

■ Solid Oxide Fuel Cell (SOFC)

■ Direct methanol fuel cell

Lithium-Air Open-Cycle Battery System

The lithium-air reaction consumes oxygen from air or from a supply tank. The chemical reaction taking place in the system is [21]:

$$2Li + O_2 \rightarrow Li_2O_2 \tag{2.12}$$

The theoretical energy density of this reaction is 5200 Wh/kg and this technology is anticipated to be market-ready in 2030 [21].
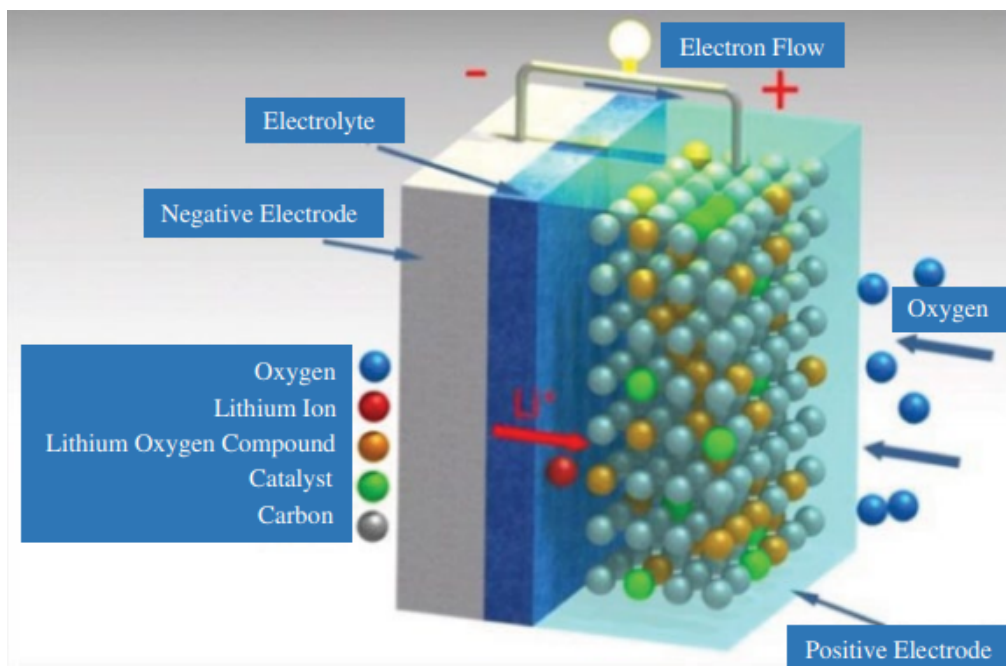
Figure 2.12: Lithium-air battery system. [21]

Chapter 3

Theory of Recuperative Propulsion

3.1 Propulsion Efficiency in Froude-Rankine Model
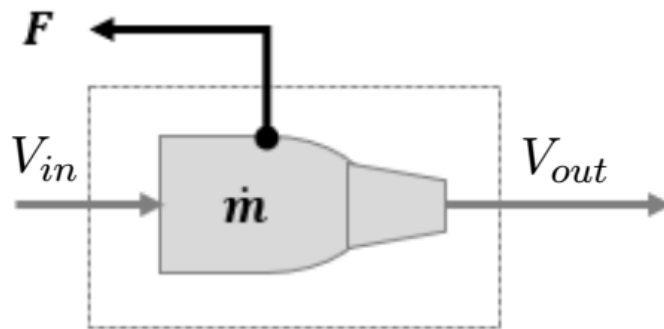
Figure 3.1: Schematic view of Froude-Rankine Propulsion Model

This theory was developed in the late 19th century and is also known as momentum actuator theory. It was originally derived to describe ship propulsion, using basic laws of mechanics and Bernoulli's equation [25]. Later on, it was applied on aircraft propellers and helicopter rotors. This model is widely used to explain the thrust generation of jet engines in many propulsion textbooks, for instance in *Jet Propulsion* by *Nicholas Cumpsty, Cambridge University Press* [14]. As it is a very low fidelity model, the real propeller is substituted by an actuator disc and the real jet engine is substituted by a black box in which the flow properties change abruptly.

FRM is a black box model dealing with mass flow rate through the engine and

inflow and outflow values of momentum and energy. The *fuel air ratio f* is set to zero in the following considerations, as an electric propulsion system does not have any fuel mass flow. Recalling the general thrust equation 2.2 and introducing Engine Power Output P [10]:

$$P_{FRM} = \frac{1}{2}\dot{m}(V_{out}^2 - V_{in}^2)$$ (3.1)

propulsive efficiency of Froude-Rankine Model can be expressed:

$$\eta_{FRM} = \frac{FV_{in}}{P_{FRM}} = \frac{\dot{m}(V_{out} - V_{in})V_{in}}{\frac{1}{2}\dot{m}(V_{out}^2 - V_{in}^2)} = \frac{2}{\frac{V_{out}}{V_{in}} + 1}$$ (3.2)

Inflow velocity is mostly determined by flight conditions, so the strategy to maximize propulsion efficiency is lowering V_{out} as much as possible. This strategy leads to extremely large diameter propellers (or high BPR in case of turbofans) if the original thrust must be conserved.

In order to plot propulsion efficiencies of different propulsion models as functions of one variable a new quantity *velocity ratio x* is introduced:

$$x = \frac{V_{out}}{V_{in}}$$ (3.3)

Then, the propulsion efficiency of FRM using *velocity ratio* is:

$$\eta_{FRM} = \frac{2}{1 + x}$$ (3.4)

3.2 Adjusted Propulsion Model
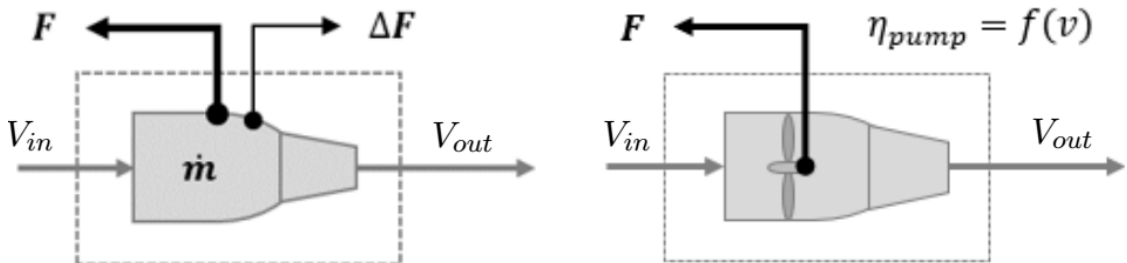
Figure 3.2: Adjusted Froude-Rankine Model. [26]

22

The external aerodynamic drag of an engine's nacelle plays an important role in its performance. On one hand, increasing the aforementioned BPR improves propulsion efficiency, but on the other hand it increases nacelle diameter and thus its drag. In order to include this drag in the consideration, the terms "installed thrust" and "uninstalled thrust" are introduced. They refer to the actual propulsive force transmitted to the aircraft by the engine and the thrust produced by the engine if it had zero external losses, respectively [20].

$$F_{installed} = F_{uninstalled} - D_{nacelle} \tag{3.5}$$

The Equation 3.5 can be rewritten using FRM (Froud-Rankine Model) and APM (Adjusted Propulsion Model) notation and with the drag expressed as a product of *mass flow rate* $\dot{m}$ and a *velocity drop due to nacelle drag* ΔV:

$$F_{APM} = F_{FRM} - \dot{m}\Delta V \tag{3.6}$$

$$F_{APM} = \dot{m}(V_{out} - V_{in} - \Delta V) \tag{3.7}$$

The power in the APM is also adjusted in comparison with the original FRM. The FRM deals with flow power, which is the change of kinetic energy of the mass flow entering and leaving the black box. The APM deals with shaft power, which is the flow power adjusted by the pump efficiency η_{pump}:

$$P_{APM} = \frac{P_{FRM}}{\eta_{pump}} \tag{3.8}$$

Thus, APM uses shaft power instead of flow power, which increases its fidelity in comparison with FRM. The pump efficiency is not a constant, it depends heavily especially on the ram pressure at cruise. The basic equation for pump efficiency is:

$$\eta_{pump} = \frac{P_{flow}}{P_{shaft}} = \frac{\Delta p Q}{P_{shaft}} \tag{3.9}$$

where Δp is a pressure difference on the impeller in [Pa] and Q is the volumetric flow rate through the pump in $[m^3.s^{-1}]$. The dynamic pressure q at the inlet exhibits quadratic growth with the cruise speed and thus decreases the pressure difference

and efficiency:

$$q = \frac{1}{2}\rho V^2 \tag{3.10}$$

Pump efficiency and pressure difference are plotted in Figure 3.3 as functions of volumetric flow rate Q. These dependencies are more complex and usually are obtained by lab measurement or by simulations for a particular pump.
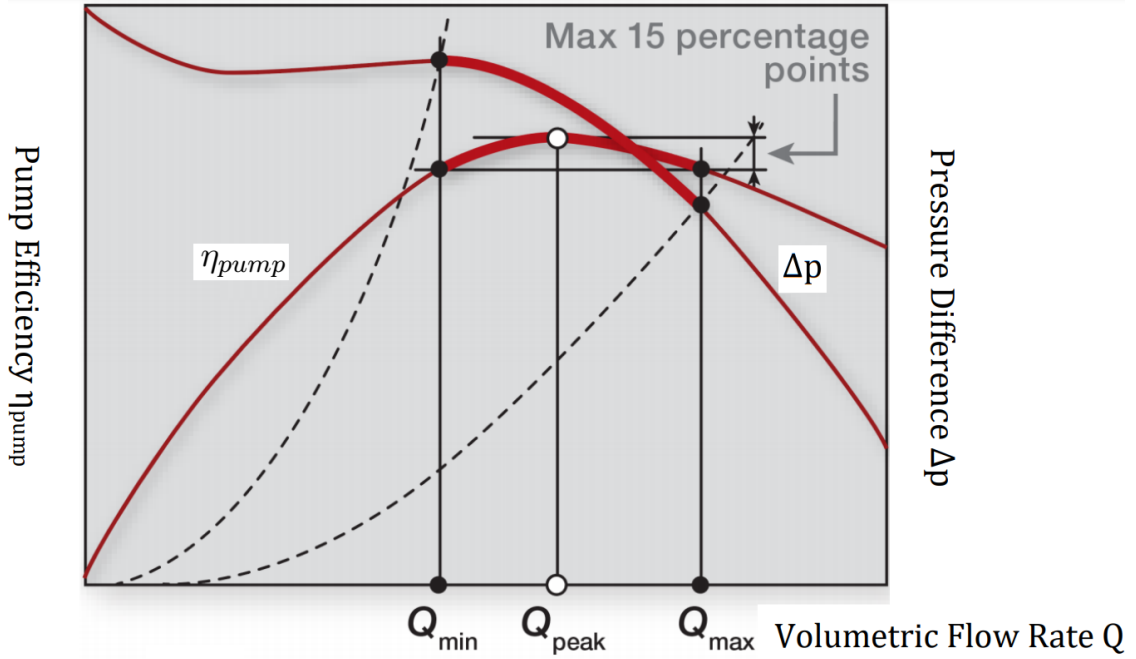
Figure 3.3: Pump efficiency and pressure difference as a function of Q. [27]

Point Q_{peak} in Figure 3.3 represents the volumetric flow rate at which the maximum efficiency is achieved. Q_{min} and Q_{max} are the volumetric flow values under and above Q_{peak} respectively, delimiting 15 % from the peak. Thus, we can define values of Q and Δp that will keep the efficiency near the optimum.

Now combining the FRM power equation 3.1 with Equation 3.8, APM's power is:

$$P_{APM} = \frac{\dot{m}}{2} \frac{(V_{out}^2 - V_{in}^2)}{\eta_{pump}} \tag{3.11}$$

As a step on the way to express the efficiency in the APM, we need to deal with the *power to thrust ratio P/F*. It is a power spent per generation of a unit of thrust. This value should be minimized as much as possible since it is a direct measure of

the efficiency:

$$\eta = \frac{V_{in}}{\frac{P}{F}} \tag{3.12}$$

Also, the P/F ratio is related to Specific Fuel Consumption (SFC)

$$SFC = \frac{\dot{m}_{fuel}}{F} \tag{3.13}$$

A new quantity *velocity change in the engine* denoted Δc is introduced to simplify the equations:

$$\Delta c = V_{out} - V_{in} \tag{3.14}$$

The P/F ratio can be expressed using equations 3.8, 3.7, and 2.2. After simplifying it can be written as a multiple of P/F ratio of FRM:

$$\frac{P_{APM}}{F_{APM}} = \frac{P_{FRM}}{F_{FRM}} \left(\frac{1}{1 - \frac{\Delta V}{\Delta c}} \right) \left(\frac{1}{\eta_{pump}} \right) \tag{3.15}$$

Finally, the efficiency of the APM η_{APM} is:

$$\eta_{APM} = \frac{V_{in}}{\frac{P_{APM}}{F_{APM}}} \tag{3.16}$$

Substituting for P/F ratio from 3.15 and after modification:

$$\eta_{APM} = \eta_{pump}\eta_{FRM} \left(\frac{1}{1 - \frac{\Delta V}{\Delta c}} \right) \tag{3.17}$$

or

$$\eta_{APM} = \eta_{pump} \left(\eta_{FRM} - \frac{2\frac{\Delta V}{V_{in}}}{\frac{V_{out}^2}{V_{in}^2} - 1} \right) \tag{3.18}$$

This expression can be further simplified by using velocity ratio x and by introducing a new dimensionless quantity y, which expresses relative velocity drop due to nacelle

drag:

$$y = \frac{\Delta V}{V} \tag{3.19}$$

$$\eta_{APM} = \eta_{pump} \left(\eta_{FRM} - \frac{2y}{x^2 - 1} \right) \tag{3.20}$$

Dimensionless quantity y will increase with increasing BPR, lowering the efficiency of the APM model. Velocity ratio x will decrease with increasing BPR and finally approach 1 with "infinite" BPR.

3.3 Comparison of Froude-Rankine and Adjusted Propulsion Models

To compare both FRM and APM models, their efficiencies can be plotted as a function of dimensionless quantities x and y introduced earlier in the text. Since x is a ratio of outflow and inflow velocities, it would theoretically go from 1 to infinity. For this reason, it's practical to plot the efficiencies as a function of the reciprocal of x, quantity $1/x$, hereafter *Normalized velocity*.

$$\frac{1}{x} = \frac{V_{in}}{V_{out}} \tag{3.21}$$

Equations 3.20 and 3.4 were used for plotting the efficiencies of both theories in the Figure 3.4.
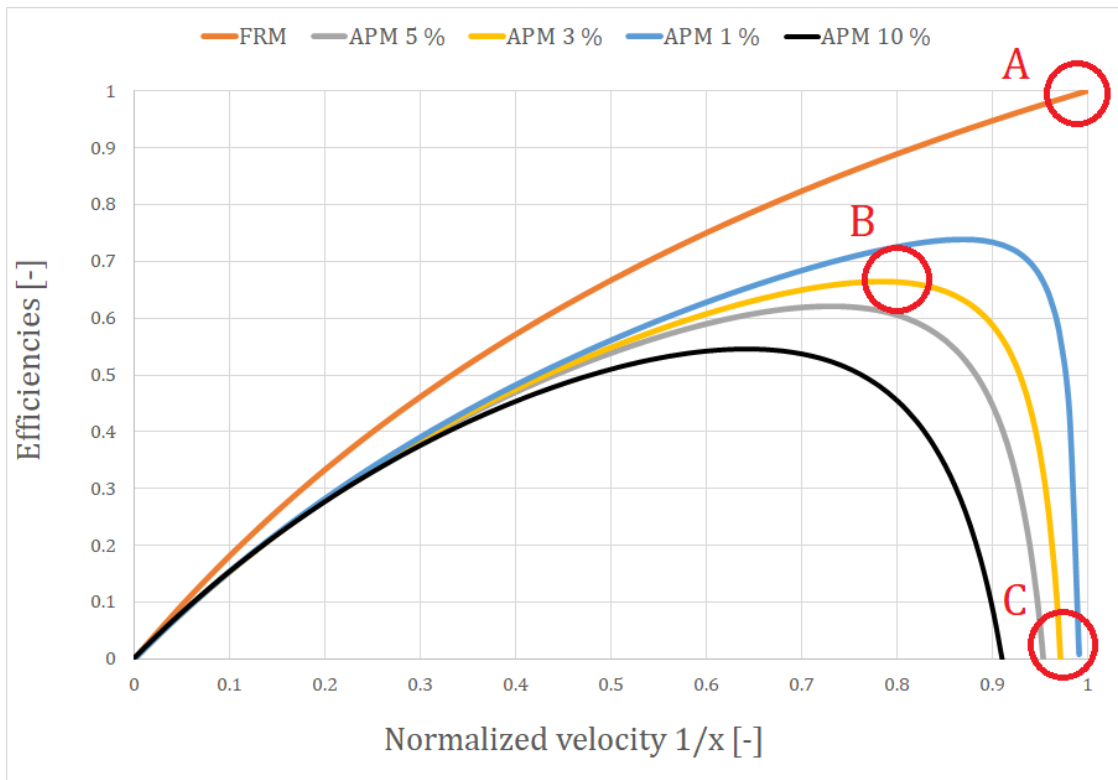
Figure 3.4: Efficiencies of FRM and APM models as a function of Normalized velocity.

Normalized velocity runs from 0 to 1, where 0 means hypothetically infinite outflow velocity (or zero inflow velocity at the start) and 1 means equal inflow and outflow velocities.

The interpretation of marked points in Figure 3.4:

- Point A - the FRM shows efficiency equal to 1, but the thrust is equal to zero → pointless hypothetical situation. This is the reason why the classical FRM theory fails to represent the reality here. An infinite diameter propeller or infinite BPR turbofan are not the key to high efficiency in real-world conditions.

- Point B - the peak efficiency of the APM model (different for different values of y). This means that increasing BPR doesn't improve efficiency past this point due to the enormous drag of nacelle.

- Point C - the APM model reaches zero efficiency. In other words, all of the engine's thrust is spent to push the enormous nacelle through the atmosphere. It's evident that this case occurs earlier for larger proportional drags (y value).

There are two quantities in Equation 3.20, pump efficiency η_{pump} and velocity drop due to the nacelle drag y which haven't been expressed in numbers yet. For plotting efficiencies, η_{pump} has been set at 0.85. The APM efficiencies are plotted for four values of dimensionless quantity y: 1, 3, 5, and 10 percent, which are relevant numbers for nacelle drag, according to sources [28]. These values of course can slightly differ, which would also change the position of peak maximum efficiency, but the shape of the curve stays roughly the same. For the aforementioned values, the efficiency peak (breakpoint) comes at normalized velocity from approx. 0.65 to 0.85, depending on the respective y value. The increasing efficiency loss due to nacelle drag is caused mostly by the fraction subtracted from η_{FRM} in Equation 3.20. Call this fraction *Efficiency loss due to nacelle drag η_{loss}*

$$\eta_{loss} = \frac{2y}{x^2 - 1} \tag{3.22}$$

By plotting this quantity against the Normalized velocity for the same values of y as in Figure 3.4, the effect of the nacelle drag is obvious. The efficiency loss reaches 100 % between normalized velocities 0.9 and 1 depending on y value, which technically means that the gigantic engine is incapable of providing any thrust to the aircraft.

Figure 3.5: Efficiency loss due to nacelle drag as a function of Normalized velocity.

3.4 Static Recuperation Model
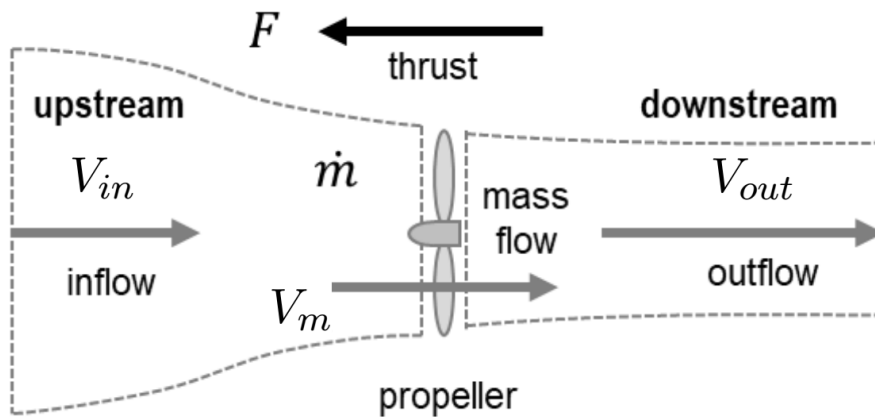
Figure 3.6: Propeller with separated upstream and downstream [29]

Figure 3.6 divides the flow to upstream and downstream. V_m is the mean velocity at propeller defined as:

$$V_m = \frac{V_{in} + V_{out}}{2} \tag{3.23}$$

Rotating propeller blades create higher static pressure at surfaces pointing backwards and lower pressure at the front surfaces by the mechanism also known from lift generation on wing. The downstream section doesn't bring anything new, the air is just accelerated (pushed) backwards from the higher pressure area behind the propeller.

On the contrary, the process that takes place upstream enables the energy recuperation from ambient air which will be elaborated later on in this text. The idea is that flow energy upstream of the propeller doesn't come from a "pull" by the propeller, but from a "push" by the ambient air [29]. The air flows into the pressure sink in front of the propeller. The idea of static recuperation is to put static blades to the inflow. The wind flowing into the pressure sink caused by the propeller will act on the static blades, generating additional thrust, if the blades are designed properly.
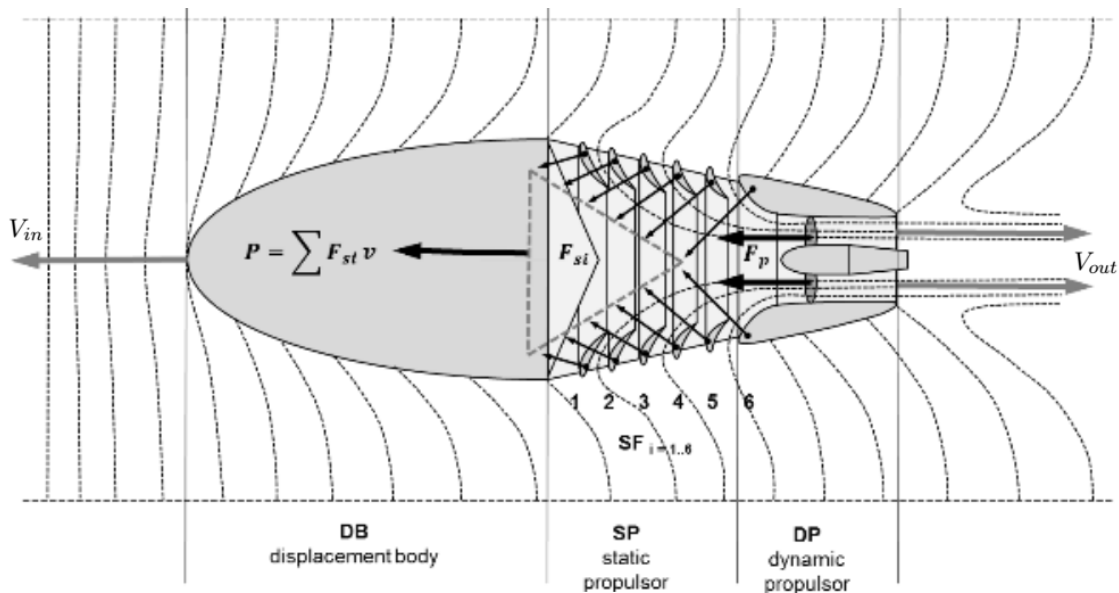
Figure 3.7: Scheme of the static recuperation principle. [26]

Another advantage of this propulsion system is its installation on aircraft. Unlike the classical jet engine, it's not to be installed on the aircraft's wing or

anywhere where ram pressure acts on it. Thanks to its special inlet, it can be built into the fuselage, entirely eliminating the aforementioned nacelle drag and decreasing the total drag rapidly.

3.4.1 Thermodynamics of the Static Recuperation Model

The laws of thermodynamics govern the relationship between the state variables of the gas, namely density ρ, pressure p, absolute temperature T, entropy s, internal energy u, and derived properties such as enthalpy h and specific heats at constant pressure and volume, c_p and c_v, respectively [20]. Following considerations work with the ideal gas model, which can be described by the equation of state:

$$p = \rho R T \tag{3.24}$$

R is the gas constant which can be determined using universal gas constant $\bar{R} = 8.314 \ JK^{-1}mol^{-1}$ and molar mass of the particular gas M:

$$R = \frac{\bar{R}}{M} \tag{3.25}$$

for air, the gas constant is: $R_{air} = 286.65 \ JK^{-1}mol^{-1}$ [20]. Enthalpy is a derived property of a thermodynamic system defined as the sum of the system's internal energy and the product of its pressure and volume. Expressed in specific (per unit of mass) quantities:

$$h = u + pv \tag{3.26}$$

where v is specific volume $[m^3kg^{-1}]$. The differential change of enthalpy and internal energy can be expressed using specific heats at constant pressure and volume, respectively:

$$dh = c_p dT \tag{3.27}$$

$$du = c_v dT \tag{3.28}$$

A simplifying assumption of constant specific heats is often applied to describe gas behavior in a narrow temperature range [20]:

$$c_p = constant, \ c_v = constant \tag{3.29}$$

and the gas is then referred to as *calorically perfect gas.* The relationship between the two specific heats can be expressed using the gas constant:

$$c_p = c_v + R \tag{3.30}$$

or using the *heat capacity ratio κ*

$$\kappa = \frac{c_p}{c_v} \tag{3.31}$$

For all diatomic gases at normal temperatures (near room temperatures), the heat capacity ratio is equal to $\kappa = \frac{7}{5} = 1.4$. At high temperatures, molecular vibrational modes and the excitation of electrons add to the degrees of freedom, and that lowers κ. κ can be considered constant for most electric propulsion computations.

Going back to the static recuperation model. Since there is no heat exchange at the inflow, the process is adiabatic. Introducing a new total quantity, the total enthalpy h_t, which is constant for the adiabatic processes

$$h_t = h + \frac{c^2}{2} = const. \tag{3.32}$$

The velocity of the flow is now denoted c, since v usually stands for specific volume in thermodynamics. Fraction $\frac{c^2}{2}$ represents the kinetic energy of the flow, denoted e. Then:

$$h_t = h + e = const. \tag{3.33}$$

Integrating the Equations 3.27 and 3.28 with the condition of constant specific heats (Eq. 3.29) the expressions for the change of enthalpy and internal energy are:

$$\Delta h = c_p \Delta T \tag{3.34}$$

$$\Delta u = c_v \Delta T \tag{3.35}$$

Using these equations and the definition of the heat capacity ratio in Equation 3.31 proportion of wind energy coming from internal energy can be expressed:

$$\frac{\Delta u}{\Delta h} = \frac{c_v}{c_p} = \frac{1}{\kappa} \tag{3.36}$$

The rest of the wind's energy comes from the change of the product pv according to 3.26:

$$\frac{\Delta(pv)}{\Delta h} = \frac{\kappa - 1}{\kappa} \tag{3.37}$$

This means that approx. 71.4 % of the wind energy comes from internal energy u, causing the temperature of the flow to go down and approx. 28.6 % comes from the work done by the gas in the expansion (pv) [29]. The condition of constant total enthalpy yields for a change between station 1 (free stream) and 2 (in front of the propeller):

$$\Delta e_{21} + \Delta h_{21} = 0 \tag{3.38}$$

Combining this equation with Equation 3.34, we obtain:

$$\Delta h_{21} = -\Delta e_{21} = c_p \Delta T_{21} \tag{3.39}$$

from which it is obvious that ΔT_{21} must be always negative.

The kinetic energy of the flow can be later on used as an additional source of thrust [29]. The static recuperation principle can only be used with a propeller that is not exposed directly to the free stream, because in this case, the ram pressure (dynamic pressure) fills in the pressure sink, preventing its use for generating additional thrust. As a consequence, an entirely new propulsion system must be designed to engage the static recuperation.

Chapter 4

Design of the Static Recuperation Propulsion System

4.1 Real elements used to create the model

The design of the propulsion system was built around existing components. This strategy was chosen to ensure a better transition from the CFD simulation executed in this thesis to a real testing scenario, which unfortunately could not be done due to the Covid-19 pandemic and closed university facilities. The testing, however, may be done later on. The part determining most of the propulsion system's dimension was the impeller. A carbon fiber-filled composite impeller HET 9305 by a company *High-End Technology RC* was used to create a 3D model and consequently the CFD simulations.

Figure 4.1: High-End Technology RC's HET 9305 impeller. [30]

The most important dimension of the model determined by this impeller is the diameter of the duct in which the impeller is placed, which is 89 mm for the HET 9305. The impeller is powered by HET Typhoon 650-68-1340 brushless DC motor which is designed to be used with the HET 9305 impeller. This system of the impeller and BLDC motor nominally provides 56 N of thrust. The impeller is connected to the motor by a 5 mm diameter shaft. The details of motor's and impeller's mounting to the system are not thoroughly studied in this thesis, the impeller thrust is only used as an input to the following CFD simulations with the aim to examine the aerodynamic forces acting on the static blades. Other components of the propulsion system were built around the impeller.

4.2   CAD Model of the Propulsion System

The 3D model was created using NX 12 CAD software by Siemens. The system is intended as a test unit for this type of propulsion model which could be used on a static lab testbed a flying testbed (aircraft) or a rotating lab testbed (carousel). The system consists of three basic parts: the front body, the static blades, and the duct with the impeller.
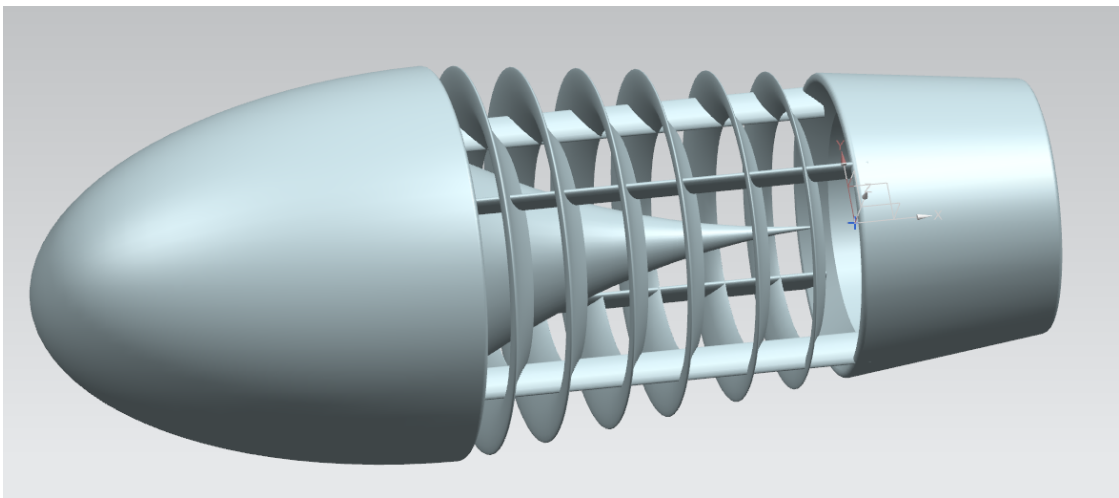
Figure 4.2: Overall view of the Propulsion System's CAD Model (NX Siemens).

35

4.2.1 Front Section

As described in previous chapters, one of the biggest static recuperation propulsion model's advantages is its installment to an aircraft. Unlike the classical engine with a front inlet, the static recuperation engine can be installed on the back section of the fuselage, eliminating the overall drag of the aircraft. Here, the entire aircraft isn't simulated, instead just an ellipsoid is used to represent the fuselage. The interior can be also used to store the motor and other electrical equipment once the system has been physically tested.

There is also a spike-shaped body connected to the ellipsoidal part in Figure 4.2. It is intended as a mean to smooth out the inner stream and to prevent excessive turbulence inside the inner parts of the inlet.

4.2.2 The Static Blades

The static blades are the essential part of the static recuperation propulsion. They were modeled by revolving six airfoil sketches about the x-axis of the model. The radii of the model are not visible in Figure 4.3 since they were created after the revolution of the sketch in the 3D model.
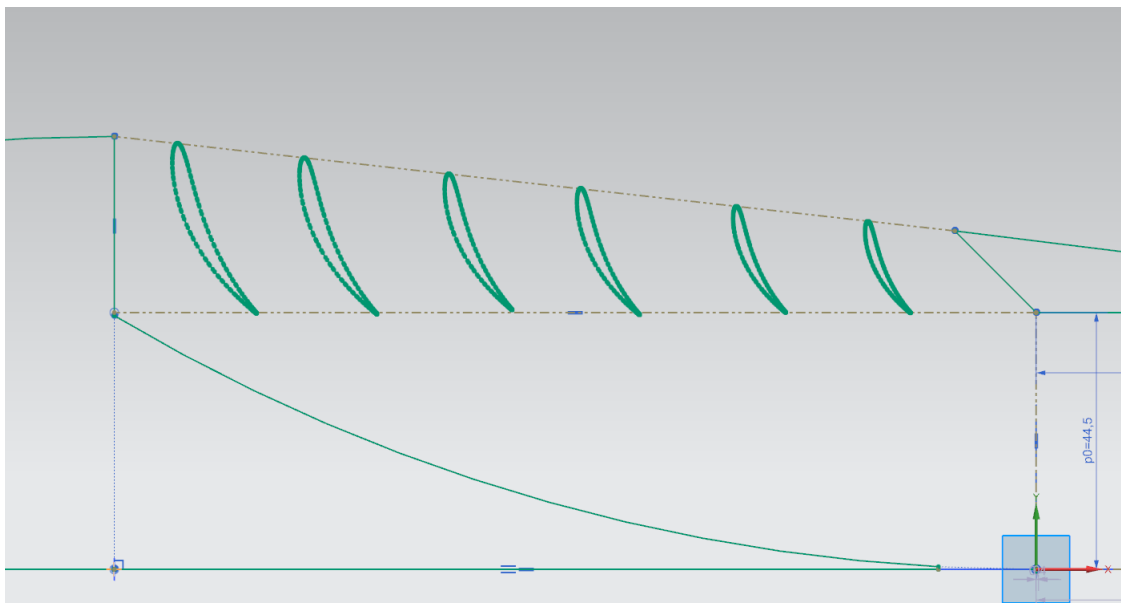
Figure 4.3: Sketch used to model Static Blades (NX Siemens).

The airfoils were designed using an online NACA 4 digit airfoil generator [31].

The airfoil's sketch was then imported to NX Siemens and copied and scaled so their arrangement is like in Figure 4.3. After revolving this sketch about the x-axis, the result is a set of six concentric rings of different diameters, each of them having an airfoil-shaped cross-section. The values used for generating the airfoil are shown in Table 4.1.

Quantity	Value
Max Camber	9.4 %
Max Camber position	50 %
Thickness	10 %

Table 4.1: Values used to generate NACA 9510 Airfoil

As shown in Figure 4.2, the blades are held in their position by four beams. These beams are also a mechanical interconnection between the front part and the duct.

■ 4.2.3 The Duct

The duct's inner diameter is determined by the impeller used to design this system and is equal to 89 mm. The interior of the duct has a shape of a cylinder.

Most of the edges in the model were rounded with a 2 mm radius as a measure against flow separation.

Chapter 5

CFD Analysis

5.1 Simulation Approach and Goal Setting

5.1.1 Introduction to CFD

Computational fluid dynamics (CFD) is one of the branches of numerical analysis used mostly for engineering applications to substitute real experiments. Its advantages in comparison with experiment are usually lower price, faster results and easy variation of boundary conditions, and other input parameters. Conversely, it's necessary to define all inputs and interpret outputs properly, otherwise, the results of CFD analysis can be grossly incorrect. The CFD analysis is often followed by proving using real world experiments.

5.1.2 Choice of Simulation Dimension

The static recuperation system examined in this thesis is, like most real-world devices, a 3D object. With today's computational power a 3D CFD analysis is not anything exceptional. However, for a case that can be considered axisymmetric a 2D simulation is a much more effective way to obtain as accurate results as possible. With the same computational power and the same computation time, the 2D axisymmetric analysis allows us to use much finer mesh and finer cells in the boundary layer at the fluid-solid interface, consequently, the simulation yields higher fidelity results. This benefit outweighs some 3D to 2D fidelity loss, caused for example by neglecting the effects of the four beams connecting the static blades

with the other parts of the assembly.

5.2 Geometry of CFD Simulation Model
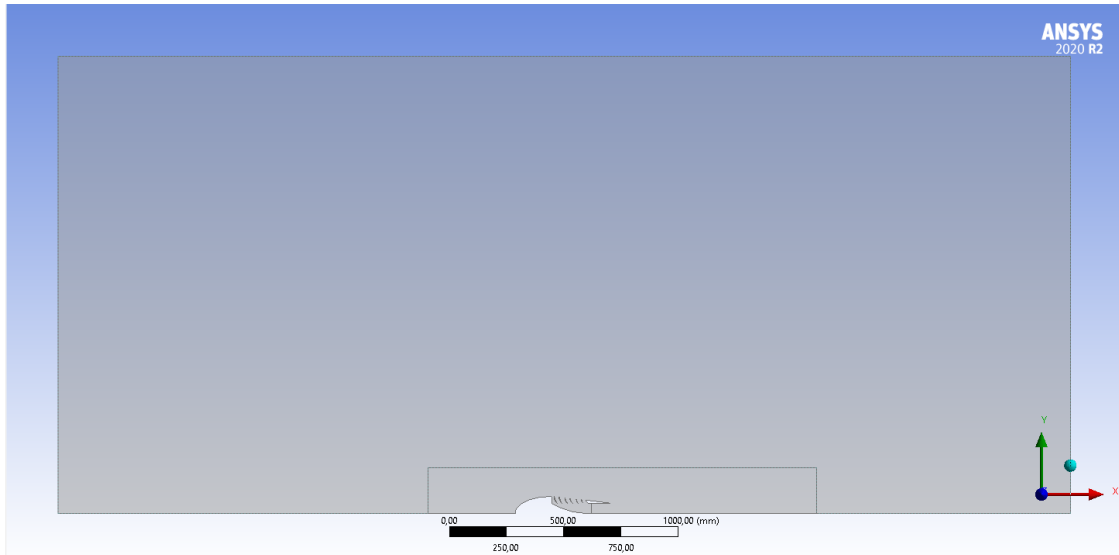
Figure 5.1: The 2D geometry used to perform the CFD Analysis.

The axisymmetric simulation requires a 2D sketch. The sketch was obtained by exporting the geometry as a .STEP file from *NX Siemens* to *DesignModeler*, a part of *ANSYS Fluent* software which was used to perform the CFD analysis. The fluid (air) has also been modeled as a rectangle above the propulsion system's cross-section. The rectangle in the 2D sketch represents a cylinder after a revolution about the x-axis. The dimensions of the fluid domain were chosen in such a way there was enough space for flow field development. The horizontal dimension was set to 4500 mm and the vertical was set to 2000 mm, which represents a cylinder of 4000 mm diameter, which is more than 28 times the largest diameter of the solid body.

39
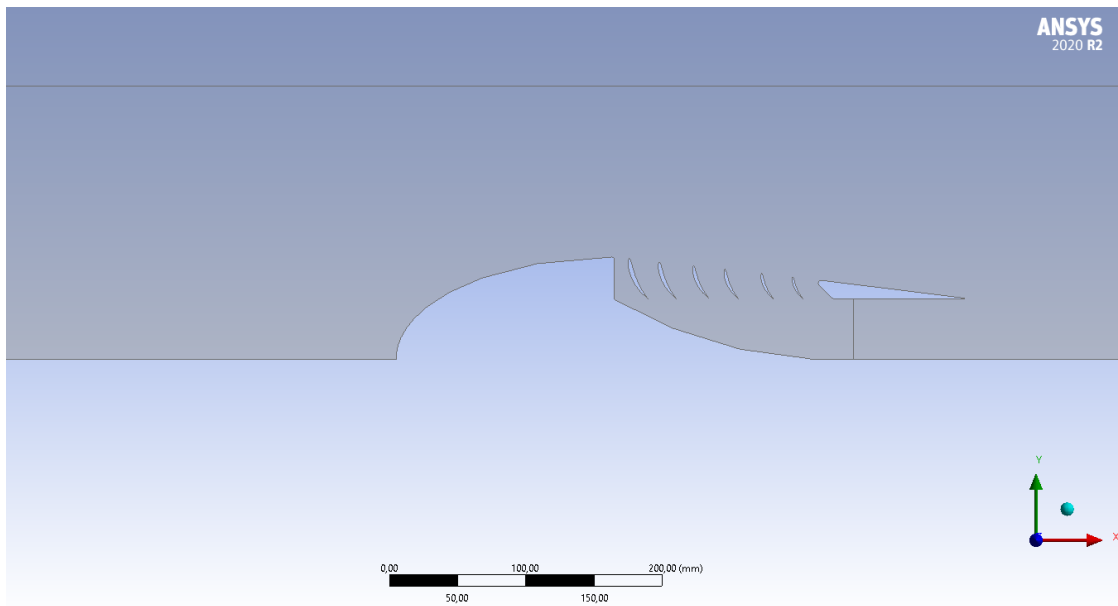
Figure 5.2: Detailed view of the simulation geometry.

Moreover, a line was added to the propulsion system's duct, which will be assigned a fan boundary condition in the next step. This boundary condition represents a simplified model of an impeller. In Figure 5.2 there's also an inner rectangle, which will be needed in meshing.

5.3   Meshing of the Model

5.3.1   About Meshing

Meshing is an essential step in a CFD simulation problem setup. The mesh needs to be fine enough to represent reality (moving fluid) properly. Per contra, the extremely fine mesh causes overly long computation times. Usually, there's a different need for mesh sizing in different parts of the geometry. The mesh should be as fine as possible near solid walls (especially in the perpendicular direction) so the solver can describe the boundary layer properly. The quadrilateral mesh was used, because it is preferable to triangular mesh for a complex CFD Simulation from the accuracy viewpoint.

5.3.2 Sizing of the Mesh

The Outer Field

The outer flow's border was set by the inner rectangle in the Geometry section. The purpose of this part of the fluid domain is to describe what happens between the inlet, outlet, and the inner zone. Since there are no solid walls or spots where flow properties change disruptively a coarser mesh of 20 mm element size is used. This mesh is still fine enough to describe the outer flow and a finer mesh of this approximately eight square meters area would unnecessarily increase the computation time.
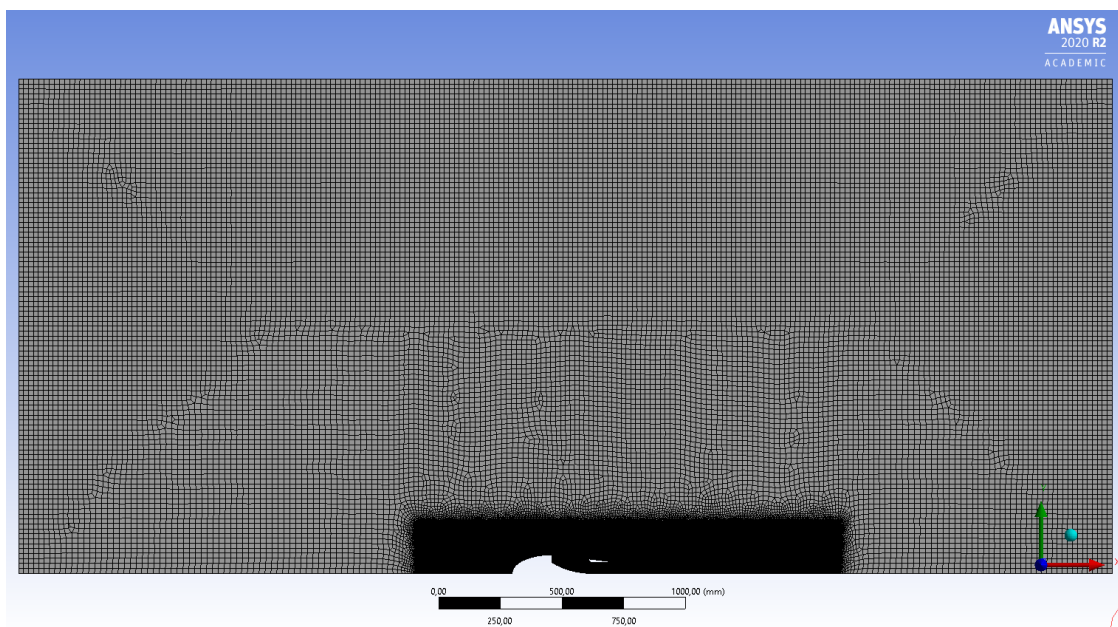
Figure 5.3: Overall view of the mesh.

The Inner Field

This area is inside the above-mentioned rectangle, which means it closely surrounds the solid walls. This part of the mesh also expands well ahead of and behind the propulsion system in the axial direction which enables a high fidelity description of the interaction of the flow from velocity inlet and solid body, as well as the stream leaving the duct on the other side. The element size in this region was set to 1 mm, meaning the area of this cell is 400 times smaller than in the outer field. This fine

mesh is needed to obtain accurate enough results around and in the interior of the propulsion system.
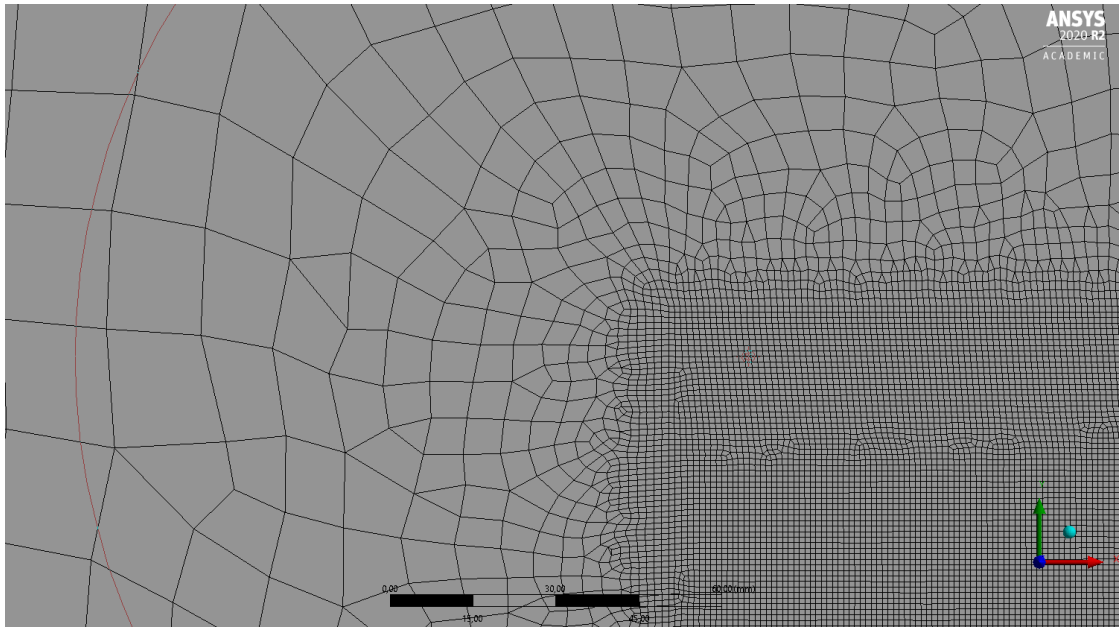
Figure 5.4: Mesh transition between the inner and outer field.

The Boundary Layer

The *inflation layer* is a tool in ANSYS Meshing designed to ease mesh creation around solid walls, where the boundary layer is expected. The sizing of this part of the mesh was a result of an iterative process in which different inflation models were applied and consequently, the boundary layer was examined. There are some parameters helping us to determine the quality of the inflation layer. For example the parameter *Yplus*. It can be obtained later on once the calculation is completed. After a few experiments, the *First Layer Thickness* inflation layer method was selected, with the first layer height of 0.02 mm and growth rate coefficient of 1.1. This inflation was applied to all fluid-solid interfaces.
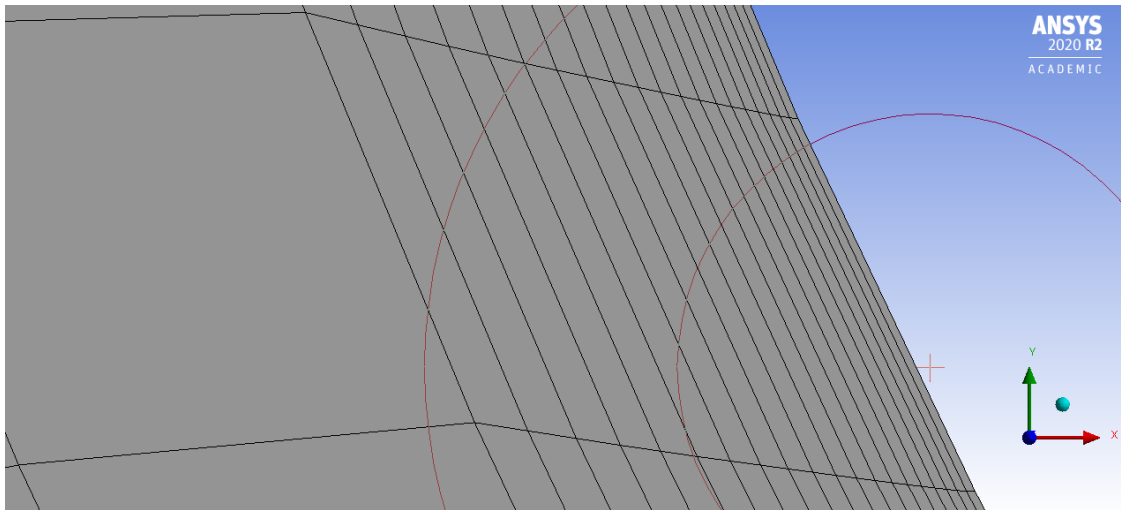
Figure 5.5: Mesh inflation at the fluid-solid interface.

The Fan Mesh

Since the impeller is represented by an internal boundary condition called fan in the CFD simulation, it will be henceforth referred to as mostly as *fan* to adopt the Fluent terminology. In the 2D axisymmetric geometry, the fan is represented by a single line segment. The fan boundary condition will be defined as a "pressure jump". As a result, a disruption in the flow field is expected. To describe the flow with acceptable accuracy, the mesh will be finer at this spot. The mesh was refined by edge sizing on the line segment with a cell size equal to 0.05 mm.
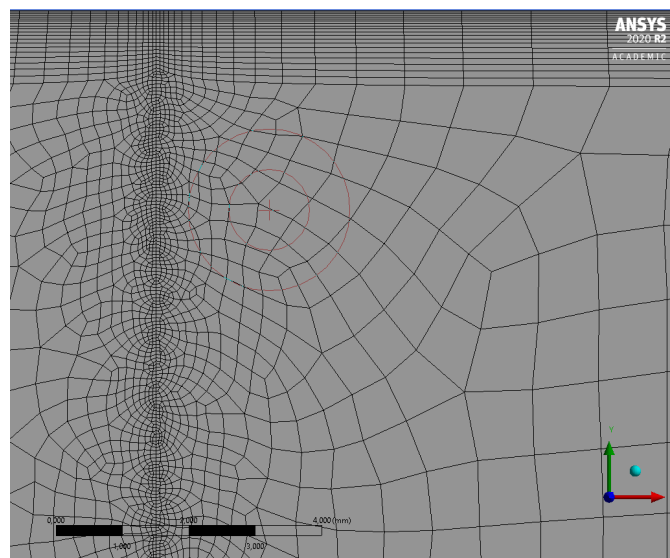
Figure 5.6: Mesh sizing on the line segment representing the fan.

43

Figure 5.7 captures all of the mesh sizing items mentioned in this section and thus provides offers a good global overview.
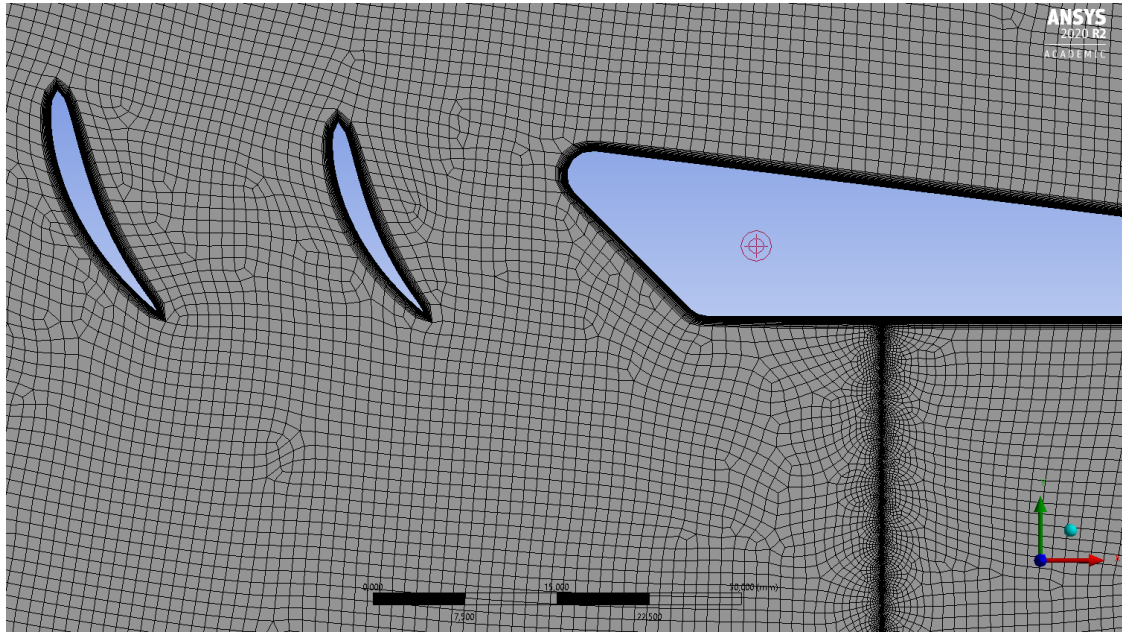
Figure 5.7: Detail of the mesh.

Mesh feature	Size [mm]
Outer field	20
Inner field	50
Inflation first layer	0.02
Fan line	0.05

Table 5.1: Mesh sizing summary

5.4 Simulation Setup

5.4.1 General

Fluent was launched with *Double Precision* in order to obtain higher fidelity results. The simulation was then switched to axisymmetrical, which allows us to simulate a real 3D problem using 2D geometry, as described earlier. At Mach numbers much less than 1.0, compressibility effects are negligible, therefore the variation of the

gas density with pressure can safely be ignored in this flow modeling [32]. Other general simulation settings are presented in Table 5.2.

Simulation setting	Value
Type	Pressure-Based
Velocity formulation	Absolute
Time	Steady
2D Space	Axisymmetric
Gravity	No
Operating pressure	101 325 [Pa]

Table 5.2: General simulation settings

5.4.2 Mesh Improvement

The simulation setup was performed directly in the Ansys Fluent graphic user interface. First of all, the mesh was improved by the built-in tool *mesh improvement*. This tool takes a defined fraction of worst-quality mesh elements (1 % was set) and improves the quality (size) of those cells.

5.4.3 The Choice of a Viscosity Model

The choice of the appropriate viscosity model has an immense impact on the simulation's results. The simulation was tested with different models, for instance, $k - \epsilon$ or $k - \omega$. Their results were consequently analyzed with emphasis on the flow parameters near walls. The quality of the viscosity model was evaluated mainly by values of Y+ (Yplus) on the fluid-wall interface and the overall quality of the flow field. The values of Y+ were consulted with the official *Fluent User's Guide* [33]. These analyses also helped to improve the mesh retrospectively. Finally, it was decided select the *Transition SST* viscosity model, which uses four equations to compute the viscosity effects. The *Transition SST* model is based on the coupling of the SST $k - \omega$ transport equations with two other transport equations, one for the intermittency and one for the transition onset criteria, in terms of momentum-thickness Reynolds number. [33].

5.4.4 Boundary Conditions Setup

The geometry entities where boundary conditions are required were assigned a name using tool *Create named selection* already in the meshing interface and thus Fluent recognized what boundary conditions they represent. For instance, a line segment with a name *fan* was automatically assigned with an internal boundary condition *fan.*
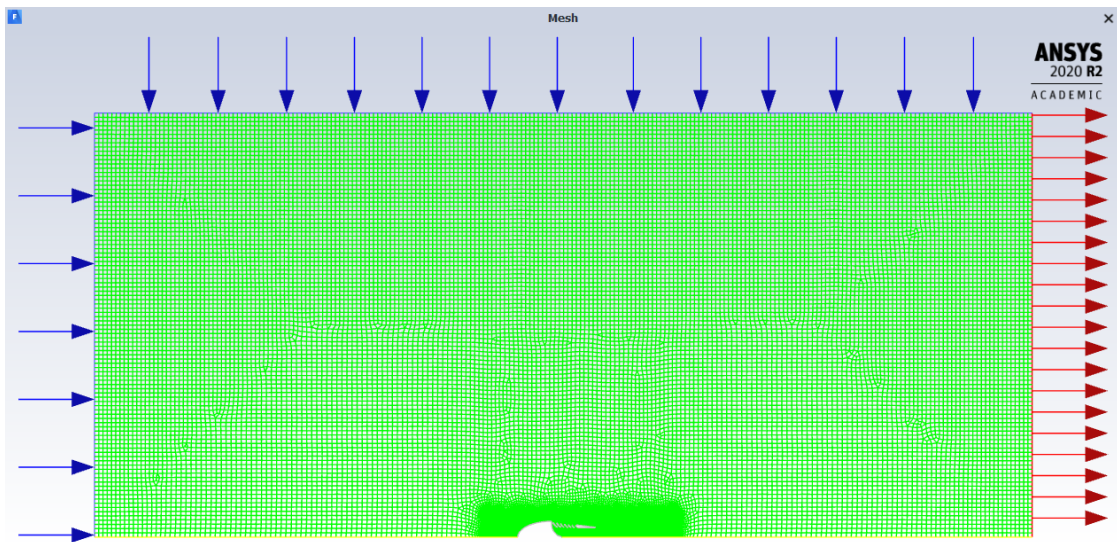
Figure 5.8: The simulation setup with defined boundary conditions.

Inlet Boundary Condition

The inlet was set as a *Velocity Inlet* with a *Velocity Specification Method* set to *Magnitude and Direction.* The inlet is defined at two of the rectangle's sides: the front one and the upper one so the air can flow into the simulation volume from both directions. The flow direction was set to purely axial, which represents a body moving through the air. The velocity magnitude was set differently for different cases. The turbulence parameters of the inlet are shown in Table 5.3

Outlet Boundary Condition

The outlet type was set to *Pressure Outlet* with *Gauge Pressure* equal to zero and with turbulence parameters same as at the inlet boundary condition.

Turbulence parameter	Value
Specification Method	Intermittency, Intensity and Viscosity Ratio
Intermittency	1
Turbulent Intensity	5 %
Turbulent Viscosity Ratio	10

Table 5.3: Inlet Turbulence Settings

Fan Boundary Condition

The fan is represented by an internal boundary condition. It is represented by a simple pressure difference which was calculated from the known parameters of the real HET 9305 impeller: its radius of 44.5 mm and thrust 56 N. The pressure difference was then calculated from the definition of pressure as the amount of force exerted per area:

$$\Delta p = \frac{F}{S} \tag{5.1}$$

$$\Delta p = \frac{F}{\pi r^2} \tag{5.2}$$

$$\Delta p = \frac{56N}{\pi \left(\frac{44.5}{1000}\right)^2 m^2} \tag{5.3}$$

$$\Delta p \approx 9001.567 Pa \approx 9kPa \tag{5.4}$$

Thus, the fan was specified as a *Pressure Jump* equal to rounded value 9000 Pascals and its direction was set to axial.

Axis

The axisymmetric problem obviously requires an axis, which was also defined as a named selection in meshing and was placed to the bottom line of the sketch. Since

there are no blades in the model of fan, the impact of the internal pressure to the shaft power cannot be studied. This simple fan representation was chosen to keep the required computational power reasonable, even though there is some fidelity loss.

■ **Walls**

Each of the blades was assigned with its own boundary condition with the view of an easier evaluation of forces later on. The rest of the solid surfaces were united to one boundary condition and forces acting on them will be also examined in the post-processing.

■ **5.4.5   Running the CFD Calculation**

Firstly, the *Hybrid Initialization* was performed to obtain the initial values for the calculation. Afterwards, the convergence check was disabled and the number of iterations was set to 1000. Since the mesh is quite fine, the parallel computation running on 4 cores of an Intel Core i5 CPU took more than an hour. Almost all of the residuals fell down quite quickly, most of them ended up around 10^{-6}, the continuity residual which ended up highest was equal little less than 10^{-3}.
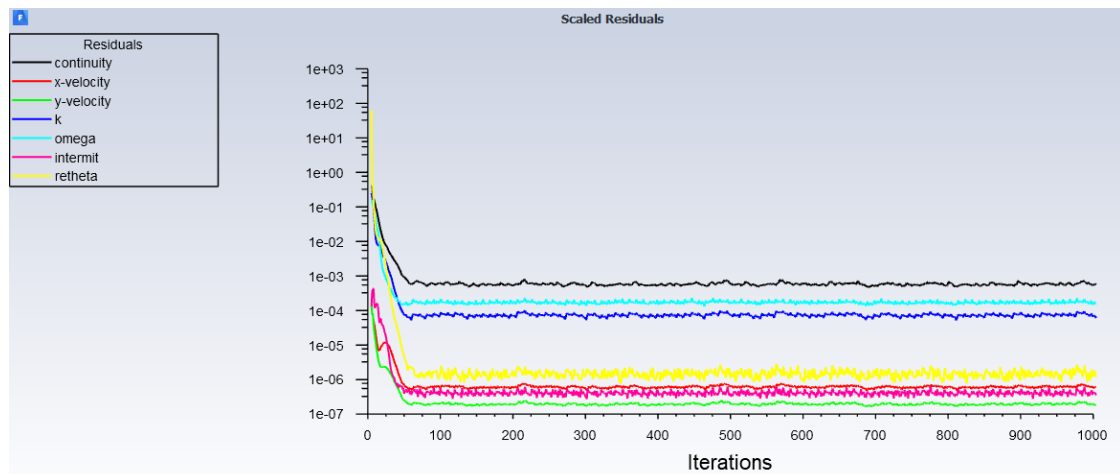
Figure 5.9: Scaled residuals of the CFD calculation.

5.5 Results of the CFD Simulation

The simulation was run in this configuration for different inlet velocity magnitudes (i.e. flight speeds). The main result of each simulation was a *force report* which is one of Fluent's features able to calculate pressure and viscous forces on selected surfaces (*walls* in the Fluent terminology). Thanks to the named selection created already in *meshing*, it will be now easy to evaluate forces acting on every single blade separately. To make results clearer, the blades were assigned numbers from 1 to 6 from left to right as shown in Figure 5.10.
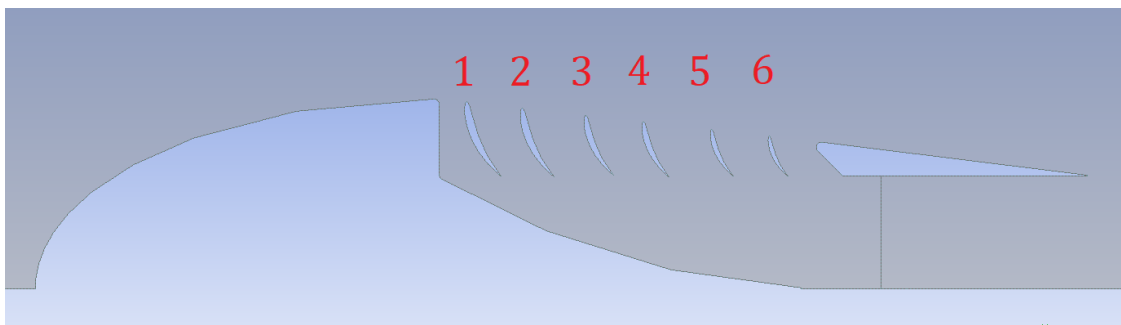
Figure 5.10: Numbering of the blades.

5.5.1 Contours of the Flow
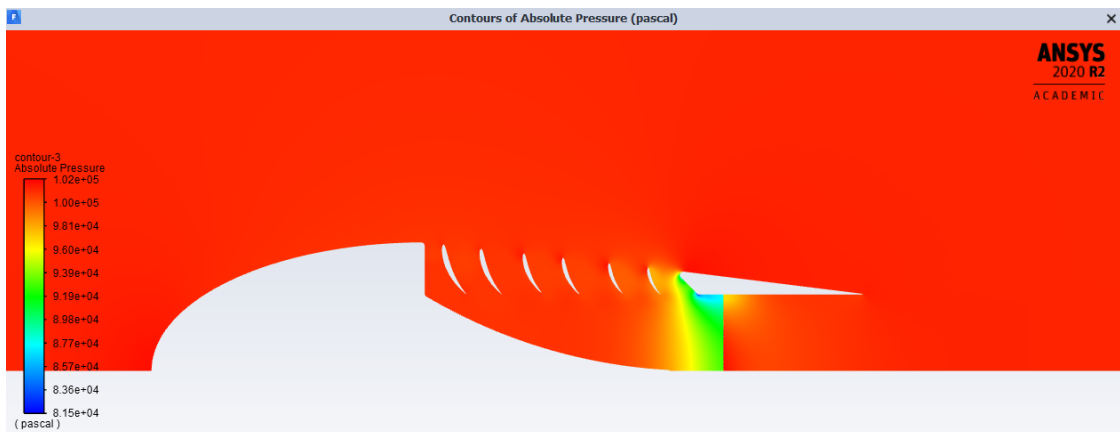
Figure 5.11: Original model: Contours of absolute pressure in the flow.

49
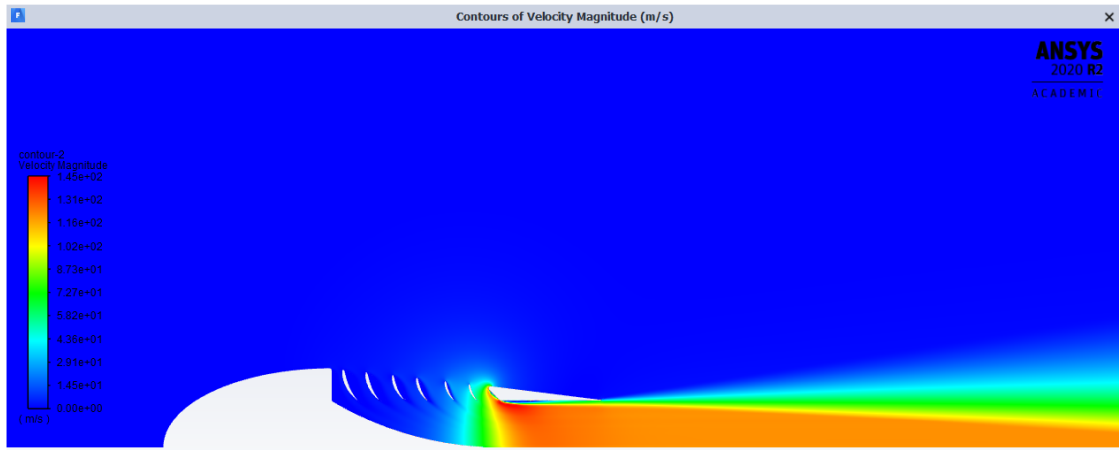
Figure 5.12: Original model: Detail view of velocity magnitude in the flow.

Another contours of the flow are presented at the end of this thesis in Appendix C.

5.5.2 Forces Acting on the Blades

The analysis was performed for different inlet velocities, starting from zero (take-off or static testbed) to 50 m/s with a step of 10 m/s. Unfortunately, it turned out that starting from zero inlet velocity, the static blades had the opposite effect than intended, moreover this effect increased with increasing velocity. This means that the direction of resulting forces on the blades was oriented *against* the desirable thrust direction. Now the results of this simulation will be presented and subsequently, the optimization steps will be proposed in order to improve the results. The forces in the following tables are the axial components of the forces and the positive direction is the direction of thrust (i.e. to the left for all the pictures in this paper).

Blade No.	Pressure forces [N]	Viscous forces [N]	Total forces [N]
Blade 1	-0.017125667	-0.00053883	-0.017664498
Blade 2	-0.094990817	-0.001055021	-0.096045838
Blade 3	-0.23760019	-0.002072357	-0.23967255
Blade 4	-0.62972568	-0.004429159	-0.63415484
Blade 5	-1.4360554	-0.01116711	-1.4472226
Blade 6	-1.0320446	-0.045920899	-1.0779655
Total	**-3.447542354**	**-0.065183377**	**-3.512725826**

Table 5.4: Original model: Forces acting on blades with zero inlet velocity.

Blade No.	Pressure forces [N]	Viscous forces [N]	Total forces [N]
Blade 1	-0.099015349	-0.003608576	-0.10262392
Blade 2	-0.15342711	-0.003218487	-0.1566456
Blade 3	-0.67922992	-0.005221609	-0.68445153
Blade 4	-1.162722	-0.007122294	-1.1698443
Blade 5	-3.0608803	-0.014555502	-3.0754358
Blade 6	-4.074166	-0.039391615	-4.1135576
Total	**-9.229440679**	**-0.073118082**	**-9.30255875**

Table 5.5: Original model: Forces acting on blades with inlet velocity equal to 10 m/s.

Blade No.	Pressure forces [N]	Viscous forces [N]	Total forces [N]
Blade 1	-0.067765517	-0.007832419	-0.075597936
Blade 2	-0.004455543	-0.005471877	-0.00992742
Blade 3	-1.225691	-0.009776701	-1.2354677
Blade 4	-1.4446512	-0.011142697	-1.4557939
Blade 5	-4.1207588	-0.020606926	-4.1413657
Blade 6	-7.6652077	-0.032877971	-7.6980857
Total	**-14.52852976**	**-0.087708591**	**-14.61623836**

Table 5.6: Original model: Forces acting on blades with inlet velocity equal to 20 m/s.

Blade No.	Pressure forces [N]	Viscous forces [N]	Total forces [N]
Blade 1	-1.1581913	0.008236119	-1.1499552
Blade 2	0.14255576	0.002973331	0.14552909
Blade 3	-1.9603101	-0.01706509	-1.9773752
Blade 4	-1.5591155	-0.017942214	-1.5770577
Blade 5	-5.1210851	-0.026619552	-5.1477047
Blade 6	-10.376455	-0.033993374	-10.410448
Total	**-20.03260124**	**-0.08441078**	**-20.11701171**

Table 5.7: Original model: Forces acting on blades with inlet velocity equal to 30 m/s.

Blade No.	Pressure forces [N]	Viscous forces [N]	Total forces [N]
Blade 1	0.22049021	-0.005219089	0.21527112
Blade 2	-1.5924443	-0.001645613	-1.5940899
Blade 3	-1.5076258	-0.02114573	-1.5287715
Blade 4	-2.3130028	-0.03068854	-2.3436913
Blade 5	-5.7269209	-0.03572011	-5.762641
Blade 6	-12.108959	-0.038895891	-12.147855
Total	**-23.02846259**	**-0.133314973**	**-23.16177758**

Table 5.8: Original model: Forces acting on blades with inlet velocity equal to 40 m/s.

Blade No.	Pressure forces [N]	Viscous forces [N]	Total forces [N]
Blade 1	-1.6370186	-0.000757606	-1.6377762
Blade 2	-2.1051371	0.012385691	-2.0927515
Blade 3	-1.0607541	-0.003937087	-1.0646912
Blade 4	-3.6806824	-0.044829861	-3.7255123
Blade 5	-6.4447487	-0.047781338	-6.49253
Blade 6	-13.409732	-0.047803992	-13.457536
Total	**-28.3380729**	**-0.132724193**	**-28.4707972**

Table 5.9: Original model: Forces acting on blades with inlet velocity equal to 50 m/s.

5.5.3   Analysis of the CFD Simulation Results of the Original Model

Table 5.10 and Figure 5.13 presents the total force (summation of forces acting on all of the blades) and the advantage related to the pure thrust of the impeller (56 N). As already mentioned, these results are not satisfactory. Even for zero inlet velocity, the resultant force in the axial direction points in the opposite direction than desired for thrust. Then, with increasing velocity, also the drag (i.e. negative thrust) of the blades increases roughly linearly.

V [m/s]	0	10	20	30	40	50
Total force [N]	-3.51	-9.30	-14.62	-20.12	-23.16	-28.47
Advantage [%]	-6.27	-16.61	-26.10	-35.92	-41.36	-50.84

Table 5.10: Original model: Total forces on blades and advantage relative to pure impeller thrust.
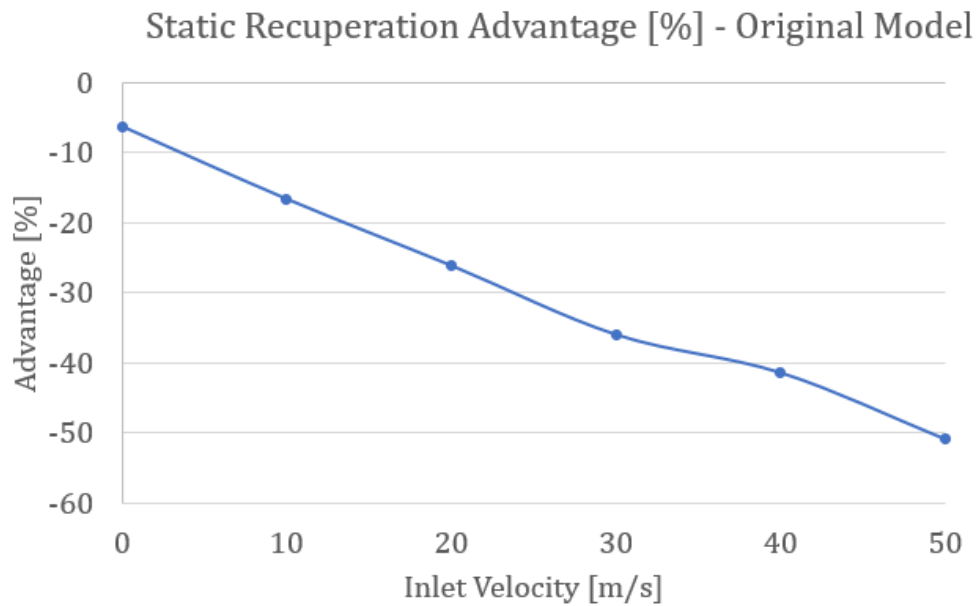
Figure 5.13: Original model: Advantage relative to impeller's thrust.

■ **The cause of reversed thrust**

Figure 5.14 shows the flow of massless particles in the fluid domain. [34] The air particles, flowing with the velocity given them at inflow, act on the blades from the front (left) side. Thus, there's locally higher pressure, leading to pressure forces in the direction opposite to thrust. The measures taken to optimize the system so it gives a *positive* thrust will be described in the following chapter.

53
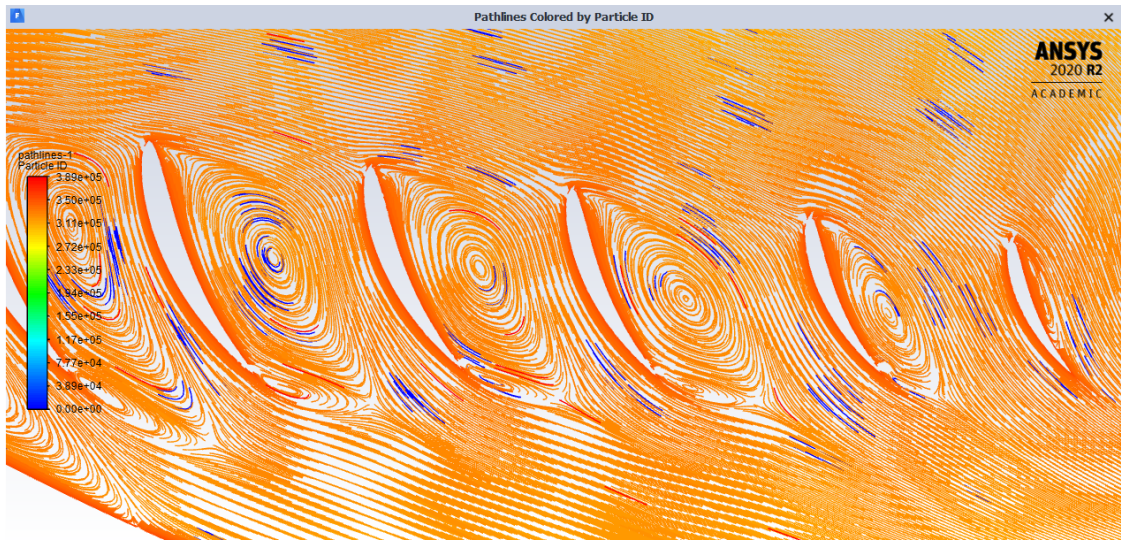
Figure 5.14: Original model: Pathlines at inflow velocity 20 m/s.

Chapter 6

Optimization of the Propulsion System

Based on previously performed analyses, an optimization of the original design was proposed. Figure 6.1 shows cross-section overlay for both original and optimized models.
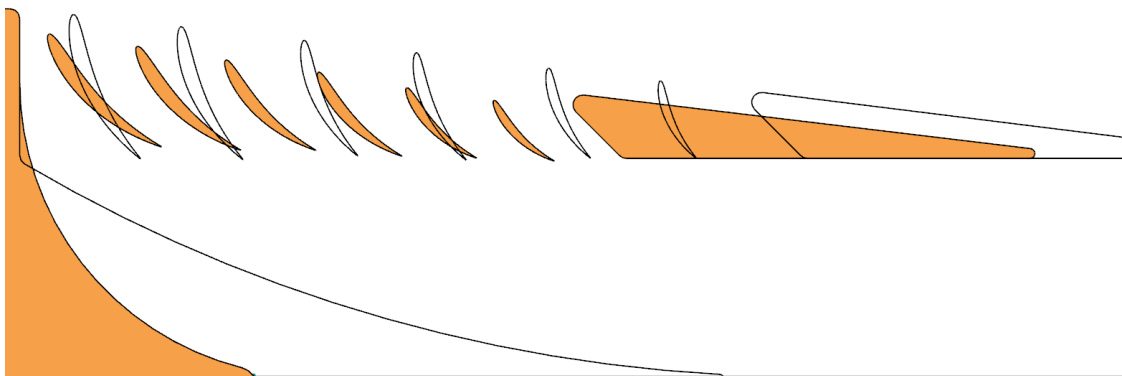
Figure 6.1: Overlay of the optimized (orange) and original model (blank).

Different options were examined and finally, it was decided to do the following:

- Relocate the static blades, specifically move them closer to the axis (downwards). Thus, the front side of the blades will be not exposed to the free stream to such an extent.

- Tilt the blades counter-clockwise. By doing this, the blades are better aligned with the inflowing pathlines. This modification helps to expose the rear side of the blades to the stream flowing into the pressure sink in front of the impeller and thereby produce useful additional thrust.

- Shorten the "central body" in the inner part of the propulsion system. This allows better and smoother airflow to the impeller and thereby increases the force acting on the correct side of the blade.

- Move the blades closer to each other. This change ensures that even the furthermost blade from the impeller (*Blade 1*) still is in the stream flowing into the pressure sink of the impeller. As a consequence of reducing the gaps between the blades, the duct moves closer to the front part of the propulsion system.

This optimization led to much better results, which will be analyzed on the following pages. The geometry of the optimized model is shown in Figure 6.2.
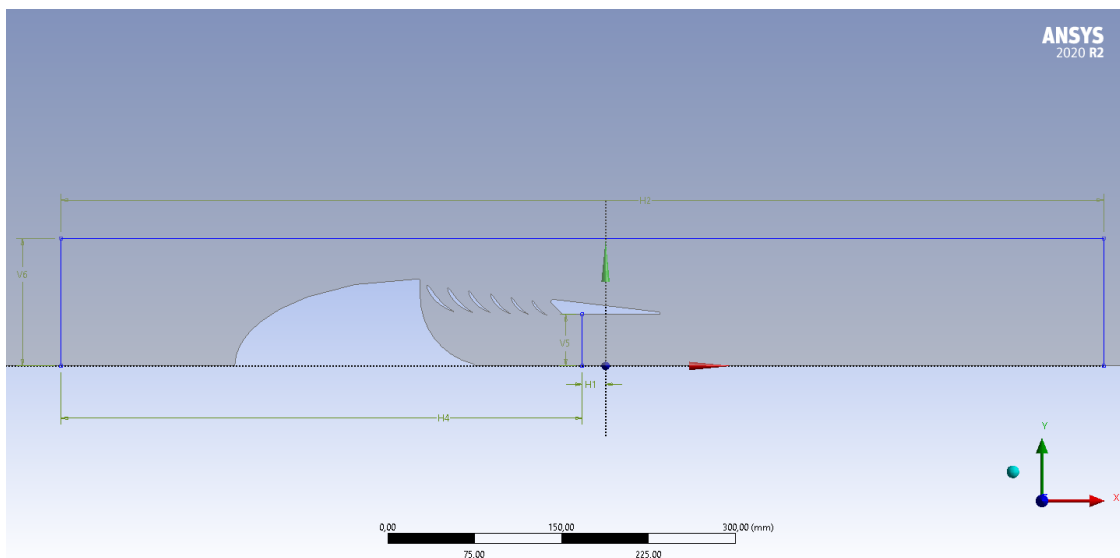
Figure 6.2: Optimized geometry
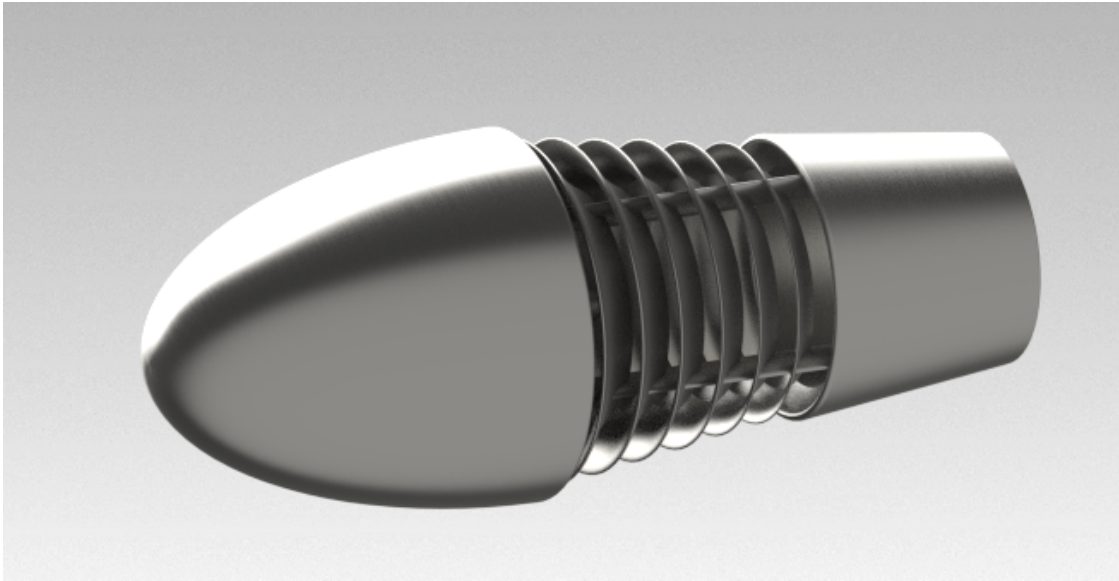
Figure 6.3: Rendered 3D model of the optimized design.

The entire process of meshing and simulation was done identically as for the original design and thereby will not be described again.

6.1 Optimized Design: Contours of the Flow

Figure 6.4 shows the pathlines in the optimized model for inlet velocity equal to 20 m/s. In contrast with the flow in the original design, there are no swirls in between the blades, and also the blades are better aligned with the shape of the pathlines.
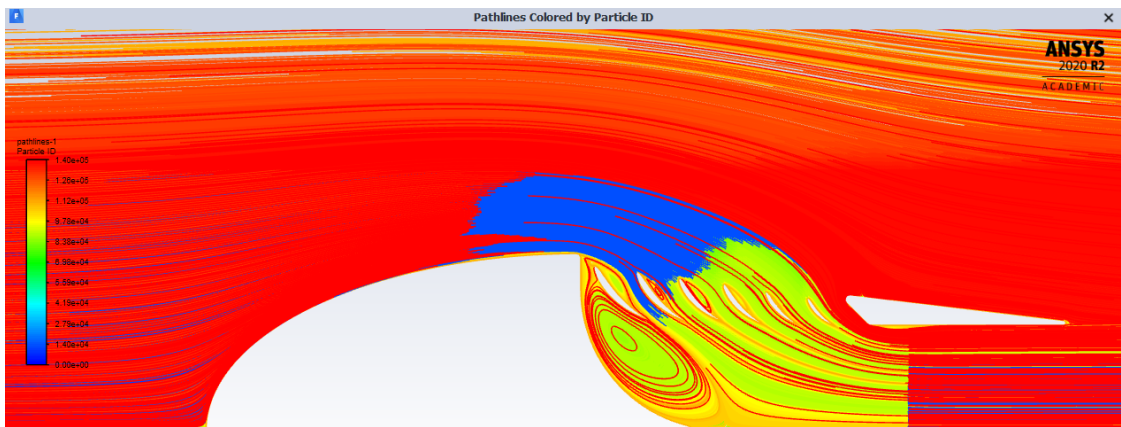
Figure 6.4: View of the pathlines for inlet velocity equal to 20 m/s.
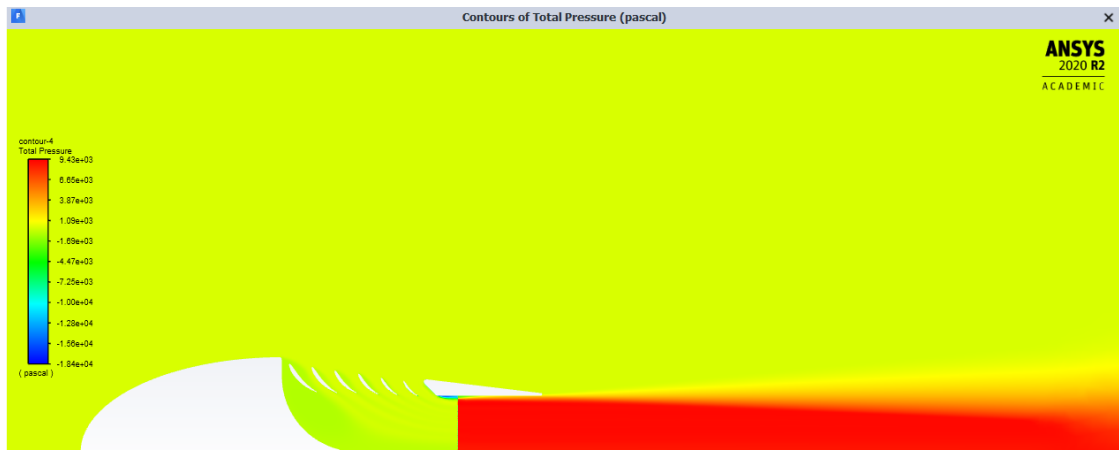
Figure 6.5: Contours of total pressure.
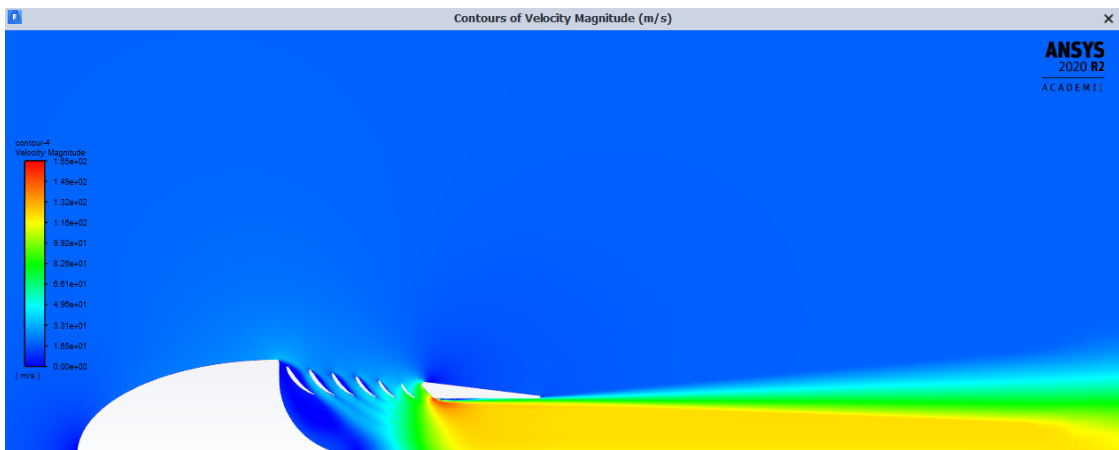
Figure 6.6: Contours of velocity magnitude.

Another flow contours for various inlet velocities are shown in the Appendix A.

6.2 Forces acting on the blades for various inlet velocities

Forces acting on the static blades are presented in this section for each inlet velocity from 0 m/s to 50 m/s. The inlet velocity was increased with a step of 5 m/s (unlike 10 m/s for the original model) in order to acquire more relevant data. Forces are divided into *viscous*, *pressure*, and *total* forces (i.e. summation of both). As

expected, the viscous forces are usually approximately two orders smaller than the pressure forces. All forces are positive in the "direction of thrust", which means axial direction.

Blade No.	Pressure forces [N]	Viscous forces [N]	Total forces [N]
Blade 1	2.7308345	-0.011780654	2.7190539
Blade 2	1.560858	-0.026863351	1.533994
Blade 3	1.0939718	-0.031705617	1.0622662
Blade 4	1.610476	-0.047852949	1.5626231
Blade 5	3.0969892	-0.064737297	3.0322519
Blade 6	6.5211375	-0.10003086	6.4211066
Total	**16.614267**	**-0.282970728**	**16.3312963**

Table 6.1: Forces acting on blades with zero inlet velocity

Blade No.	Pressure forces [N]	Viscous forces [N]	Total forces [N]
Blade 1	3.4780358	0.011939995	3.4660958
Blade 2	1.0030065	0.028388278	0.9746182
Blade 3	0.77667258	0.031216988	0.74545559
Blade 4	1.2415196	0.050587785	1.1909318
Blade 5	2.5757487	0.070490313	2.5052584
Blade 6	5.8418518	0.10982849	5.7320233
Total	**14.91683498**	**-0.302451849**	**14.61438309**

Table 6.2: Forces acting on blades with inlet velocity equal to 5 m/s

59

Blade No.	Pressure forces [N]	Viscous forces [N]	Total forces [N]
Blade 1	3.5341465	-0.023182908	3.5109636
Blade 2	0.71092104	-0.029909752	0.68101129
Blade 3	0.78518501	-0.029414	0.75577101
Blade 4	0.93037768	-0.042285686	0.888092
Blade 5	2.1979749	-0.071506615	2.1264682
Blade 6	5.1935355	-0.11679397	5.0767415
Total	**13.35214063**	**-0.313092931**	**13.0390476**

Table 6.3: Forces acting on blades with inlet velocity equal to 10 m/s

Blade No.	Pressure forces [N]	Viscous forces [N]	Total forces [N]
Blade 1	2.7554186	-0.021030924	2.7343877
Blade 2	0.66867181	-0.030689488	0.63798232
Blade 3	0.65924374	-0.026753627	0.63249012
Blade 4	0.56815582	-0.040824355	0.52733147
Blade 5	1.8324306	-0.062247636	1.7701829
Blade 6	4.5728595	-0.12265875	4.4502007
Total	**11.05678007**	**-0.30420478**	**10.75257521**

Table 6.4: Forces acting on blades with inlet velocity equal to 15 m/s

Blade No.	Pressure forces [N]	Viscous forces [N]	Total forces [N]
Blade 1	0.56322834	-0.007065387	0.55616295
Blade 2	2.2562643	-0.028904608	2.2273597
Blade 3	0.086647127	-0.02554891	0.11219604
Blade 4	0.28635515	-0.036780894	0.24957425
Blade 5	1.3617837	-0.056607871	1.3051758
Blade 6	4.1214301	-0.12832415	3.9931059
Total	**8.675708717**	**-0.28323182**	**8.21918256**

Table 6.5: Forces acting on blades with inlet velocity equal to 20 m/s

Blade No.	Pressure forces [N]	Viscous forces [N]	Total forces [N]
Blade 1	-0.5368503	-0.004754719	-0.54160502
Blade 2	3.4041521	-0.033915802	3.3702363
Blade 3	-0.55787788	-0.026163688	-0.58404157
Blade 4	0.075842566	-0.033689819	0.042152748
Blade 5	0.99028958	-0.055255978	0.9350336
Blade 6	3.6803523	-0.11944287	3.5609094
Total	**7.055908366**	**-0.273222876**	**6.782685458**

Table 6.6: Forces acting on blades with inlet velocity equal to 25 m/s

Blade No.	Pressure forces [N]	Viscous forces [N]	Total forces [N]
Blade 1	-1.1257471	0.001398893	-1.1243482
Blade 2	3.5047938	-0.042928038	3.4618657
Blade 3	-0.44898498	-0.029623435	-0.47860841
Blade 4	-0.14824404	-0.032223503	-0.18046754
Blade 5	0.64772344	-0.051385064	0.59633838
Blade 6	3.3647987	-0.10701831	3.2577804
Total	**5.79433982**	**-0.261779457**	**5.53256033**

Table 6.7: Forces acting on blades with inlet velocity equal to 30 m/s

Blade No.	Pressure forces [N]	Viscous forces [N]	Total forces [N]
Blade 1	-0.94128408	0.005843596	-0.93544048
Blade 2	2.1599091	-0.022307545	2.1376016
Blade 3	0.22144272	-0.035416071	0.18602665
Blade 4	-0.30114784	-0.032964924	-0.33411276
Blade 5	0.45257501	-0.048254413	0.40432059
Blade 6	3.0362734	-0.1023077	2.9339657
Total	**4.62776831**	**-0.235407057**	**4.3923613**

Table 6.8: Forces acting on blades with inlet velocity equal to 35 m/s

Blade No.	Pressure forces [N]	Viscous forces [N]	Total forces [N]
Blade 1	-0.90507864	-0.004529004	-0.90960764
Blade 2	0.91757316	-0.006447142	0.91112602
Blade 3	1.6574571	-0.048205583	1.6092515
Blade 4	-0.46538787	-0.03707956	-0.50246743
Blade 5	0.16550322	-0.044535347	0.12096787
Blade 6	2.638967	-0.10321629	2.5357507
Total	**4.00903397**	**-0.244012926**	**3.76502102**

Table 6.9: Forces acting on blades with inlet velocity equal to 40 m/s

Blade No.	Pressure forces [N]	Viscous forces [N]	Total forces [N]
Blade 1	-1.4158001	-0.012119412	-1.4279195
Blade 2	0.32752421	0.000145937	0.32767015
Blade 3	3.049529	-0.061437865	2.9880911
Blade 4	-0.52226689	-0.043464945	-0.56573184
Blade 5	-0.13669306	-0.041926269	-0.17861933
Blade 6	2.3394028	-0.10614556	2.2332573
Total	**3.64169596**	**-0.264948114**	**3.37674788**

Table 6.10: Forces acting on blades with inlet velocity equal to 45 m/s

Blade No.	Pressure forces [N]	Viscous forces [N]	Total forces [N]
Blade 1	-1.9366521	-0.016105564	-1.9527577
Blade 2	-0.082767091	0.007706076	-0.075061015
Blade 3	3.7991575	-0.067875034	3.7312825
Blade 4	-0.416948	-0.052483832	-0.46943183
Blade 5	-0.32656958	-0.041497429	-0.36806701
Blade 6	2.01333	-0.1058713	1.9074587
Total	**3.049550729**	**-0.276127083**	**2.773423645**

**Table 6.11:** Forces acting on blades with inlet velocity equal to 50 m/s

■ 6.3   Analysis of the Simulation Results

Since the force reports for the optimized design yield much better results in comparison with the original design, a more thorough analysis will be performed in this section. Table 6.12 shows synoptically the total forces acting on each blade in each inlet velocity configuration. The data in this table were rounded to two decimal places so the table fits the page.

V[m/s]	0	5	10	15	20	25	30	35	40	45	50
B1 [N]	2.72	3.47	3.51	2.73	0.56	-0.54	-1.12	-0.94	-0.91	-1.43	-1.95
B2 [N]	1.53	0.97	0.68	0.64	2.23	3.37	3.46	2.14	0.91	0.33	-0.08
B3 [N]	1.06	0.75	0.76	0.63	-0.11	-0.58	-0.48	0.19	1.61	2.99	3.73
B4 [N]	1.56	1.19	0.89	0.53	0.25	0.04	-0.18	-0.33	-0.50	-0.57	-0.47
B5 [N]	3.03	2.51	2.13	1.77	1.31	0.94	0.60	0.40	0.12	-0.18	-0.37
B6 [N]	6.42	5.73	5.08	4.45	3.99	3.56	3.26	2.93	2.54	2.23	1.91
Σ [N]	**16.33**	**14.61**	**13.04**	**10.75**	**8.22**	**6.78**	**5.53**	**4.39**	**3.77**	**3.38**	**2.77**

Table 6.12: Total forces acting on each blade for each velocity

The data from Table 6.12 are plotted in Figure 6.7. It shows that the performance of the static recuperation decreases with increasing velocity. The system is, however, propelled by the HET 9305 impeller, a device designed to propel aircraft models that usually operate at or under 40 m/s.
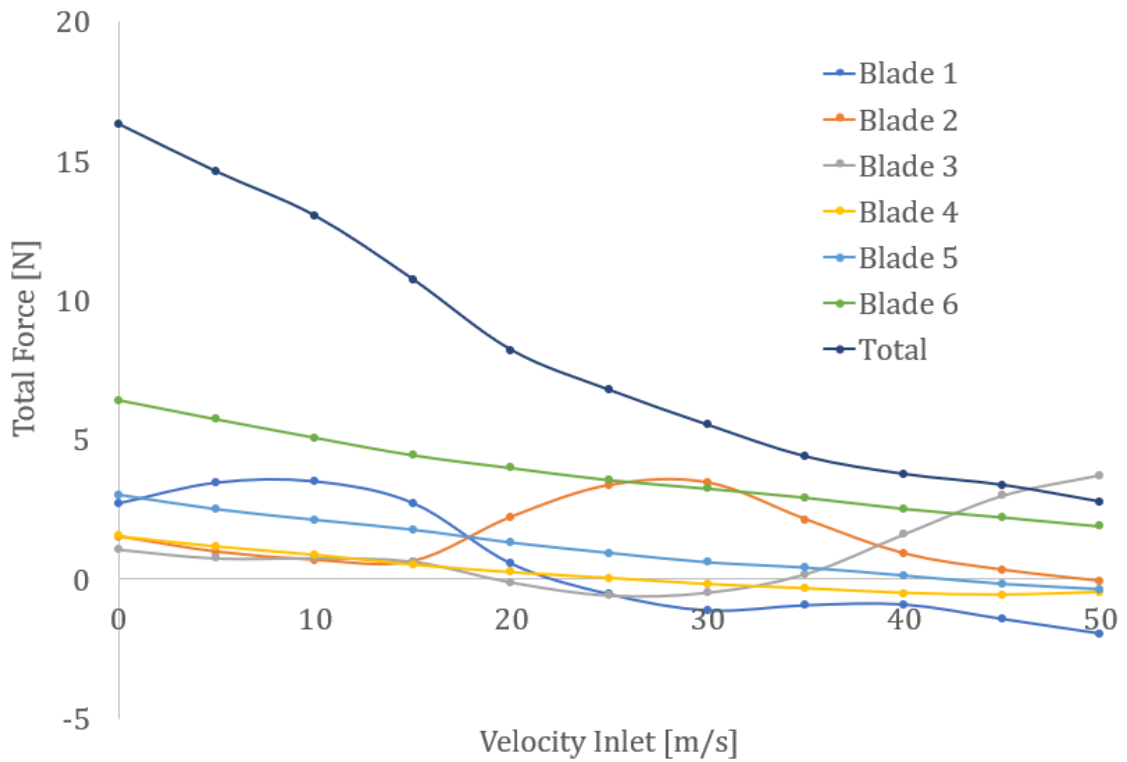
Figure 6.7: Total forces acting on each blade for each velocity.

Table 6.13 and Figure 6.8 show the contributions to the overall additional thrust of static recuperation expressed as a percentage, so the summation of each column equals 100 %. In the case of the highest flight speed of 50 m/s, the percentage of *Blade 3* exceeds 100 % as a consequence of the "negative thrust" of four other blades. Nevertheless, the sum of this column still remains 100 %. Data are plotted only up to 40 m/s velocity in Figure 6.8 for the reason of a better representation of the lower velocities. The discussion of the shape of curves in Figure 6.9 follows.

V[m/s]	0	5	10	15	20	25	30	35	40	45	50
B1 [%]	16.6	23.7	26.9	25.4	6.8	-8.0	-20.3	-21.3	-24.2	-42.3	-70.4
B2 [%]	9.4	6.7	5.2	5.9	27.1	49.7	62.6	48.7	24.2	9.7	-2.7
B3 [%]	6.5	5.1	5.8	5.9	-1.4	-8.6	-8.7	4.2	42.7	88.5	134.5
B4 [%]	9.6	8.1	6.8	4.9	3.0	0.6	-3.3	-7.6	-13.3	-16.8	-16.9
B5 [%]	18.6	17.1	16.3	16.5	15.9	13.8	10.8	9.2	3.2	-5.3	-13.3
B6 [%]	39.3	39.2	38.9	41.4	48.6	52.5	58.9	66.8	67.4	66.1	68.8

Table 6.13: Blades contribution to additional thrust expressed as a percentage.
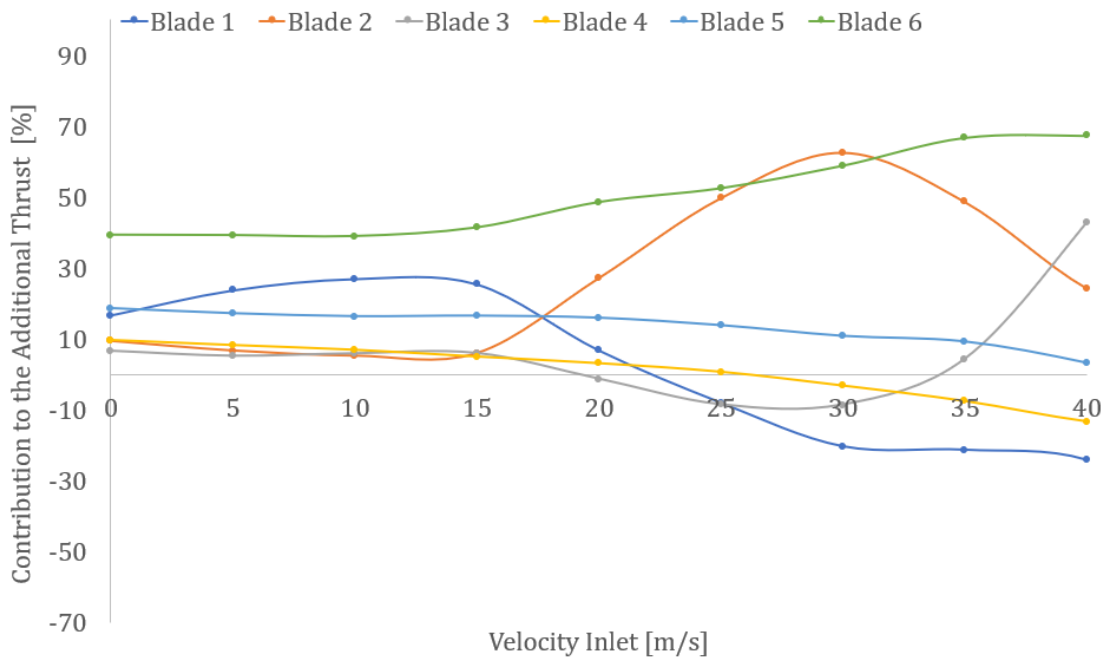
Figure 6.8: Blades contribution to additional thrust expressed as a percentage.

6.3.1 Discussion of each blade's contribution to additional thrust

The design was optimized in such a way it provides as much additional thrust as possible in a reasonable range of flight speeds. The courses of different blade's contributions to additional thrust differ significantly. Some of them are increasing with increasing velocity, some are decreasing and some of them have a local maximum or minimum.

Blade 1

Blade 1 is the furthermost from the impeller. Nevertheless, its contribution in lower velocities is one of the highest. Then, between 15 and 30 m/s, it's contribution drops, crossing the zero line at about 25 m/s, and further on it creates a little negative thrust. This negative thrust is rather significant for the highest velocity of 50 m/s when the wind stream acts on the suction side of the blade.

Blade 2

This blade contributes under 10 percent for velocities up to 10 m/s. Then, a major increase occurs, with a local maximum at 30 m/s, where the second blade makes the largest contribution of all, almost 63 %. Its contribution then drops again and it adds a negligible negative thrust (-2.7 %) for the highest speed.

Blade 3

The third blade contributes some 10 % for lower velocities, then it drops to negative numbers locally around 25 m/s. Finally, it shows a significant rise and its contribution is the highest of all for the top simulation velocity of 50 m/s.

Blade 4

This blade's contribution isn't high, but is consistent up to approximately 20 m/s. Then it drops below the horizontal axis, but its negative impact in higher velocities isn't that significant as in the case of the first blade.

Blade 5

The second closest blade to impeller shows a slow decrease from almost one-fifth of contribution to additional thrust and only adds a little negative thrust for the two of the highest velocities 45 and 50 m/s.

Blade 6

The rightmost blade performs the best of all for almost all of the velocities range. It is only outperformed by the second blade in the interval from 25 to 30 m/s.

6.3.2 Relative Improvement of Thrust With Static Recuperation

Table 6.14 Figure 6.9 expresses the advantage provided by static recuperation relative to the original thrust of the impeller, that is 56 N.

V [m/s]	0	5	10	15	20	25	30	35	40	45	50
Adv. [%]	29.16	26.10	23.28	19.20	14.68	12.11	9.88	7.84	6.72	6.03	4.95

Table 6.14: Additional thrust related to the original thrust of the impeller.
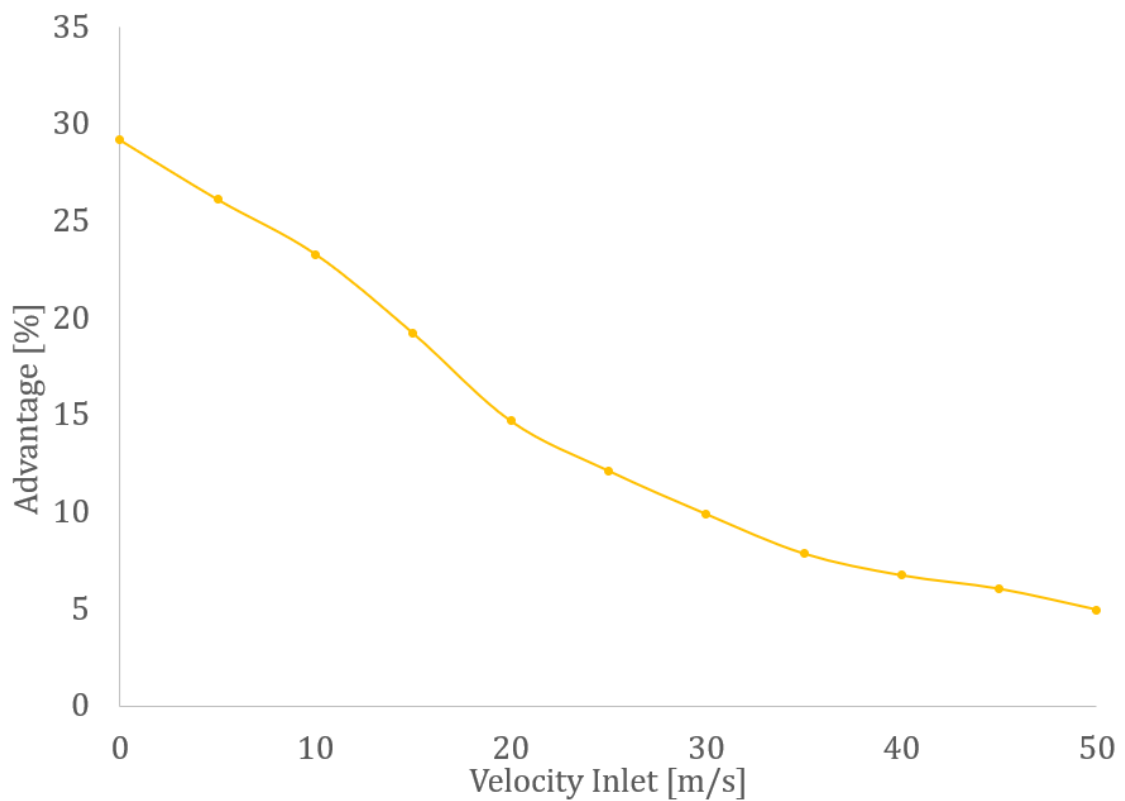
Figure 6.9: Additional thrust related to the original thrust of the impeller.

67

Chapter 7

Comparison with a Standard Propulsion System

7.1   Comparison using CFD

In this section, the recuperative system will be compared to a standard propulsion system. A new geometry and set of simulations were created for this purpose. The geometry is very similar, the only difference is its absence of the static blades as shown in Figure 7.1. Also, the simulation setup including meshing, boundary conditions, or viscosity model was identical to previously performed simulations.

The model used for this comparison doesn't represent a typical propeller (or turbofan) since in this case the impeller is not exposed to the ram pressure. The ram pressure decreases overall propulsion efficiency as described in the theoretical part of this thesis.

The flow contours for various inlet velocities are shown in the Appendix B.
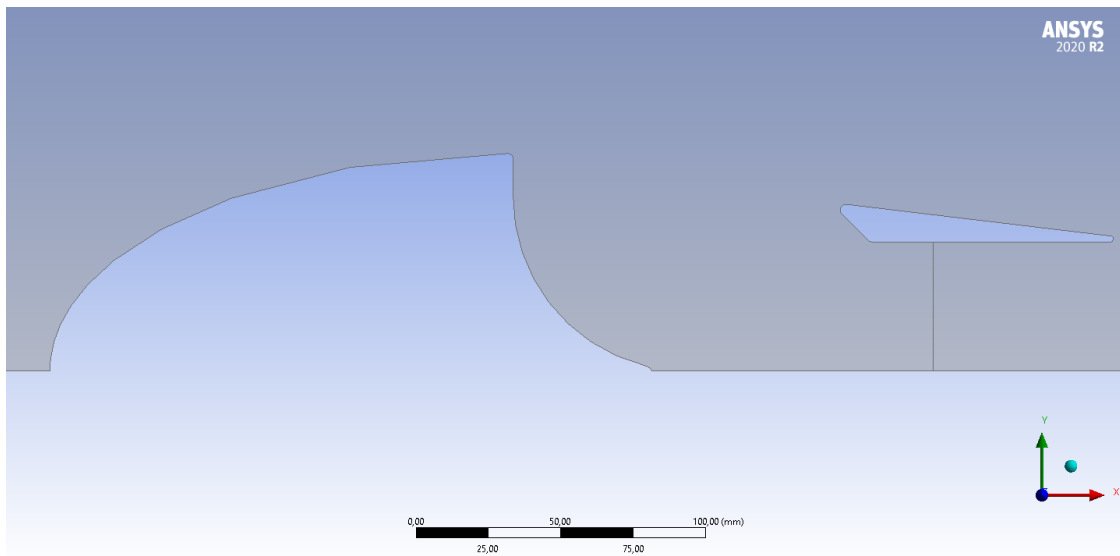
Figure 7.1: Geometry used for comparison of Recuperative and Standard propulsion systems.

The forces presented in Table 7.1 for both Recuperative and Standard propulsion system take into account the thrust of the impeller (constant of 56 N) and also all forces acting on all surfaces in the simulation, i.e. drag of the nacelle and additional thrust from the blades (if applicable).

$$F_{total} = F_{impeller} - D_{nacelle}(+F_{blades}) \tag{7.1}$$

V [m/s]	0	5	10	15	20	25	30	35	40	45	50
Impeller [N]	56	56	56	56	56	56	56	56	56	56	56
Recuperative [N]	66.5	63.4	60.3	57.4	54.5	51.6	48.8	45.9	43.0	40.2	37.3
Standard [N]	55.1	53.9	52.4	50.8	49.1	47.1	45.1	42.9	40.6	38.2	35.5
Advantage [%]	17.1	15.0	13.1	11.4	10.0	8.7	7.6	6.6	5.7	5.1	4.8

Table 7.1: Comparison of the Recuperative and Standard Propulsion system.

Figures 7.2 and 7.3 visualize the force and relative advantage data from Table 7.1 for both designs. It shows that the difference is distinct for zero flight speed (take-off) where the recuperation system's advantage is more than 17 %. With increasing speed the difference decreases, but it's still 10 % for 20 m/s and almost

6 % for 40 m/s.

Comparison of Recuperative and Standard Propulsion
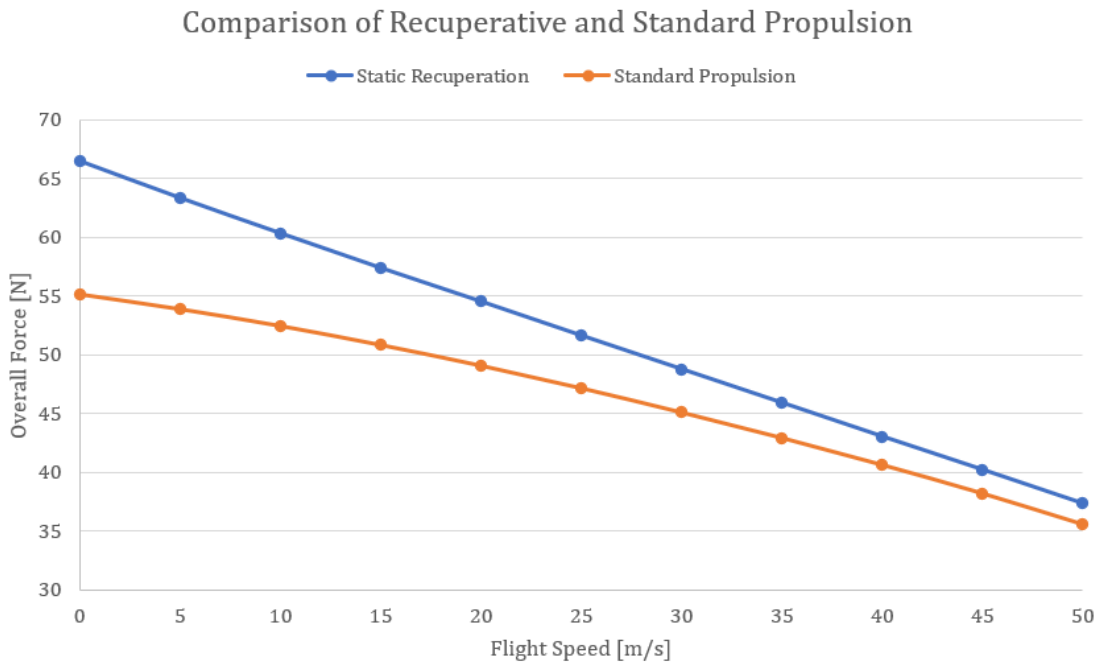
Figure 7.2: Overall thrust comparison for Recuperative and Standard propulsion.

Advantage: Recuperative vs. Standard Propulsion
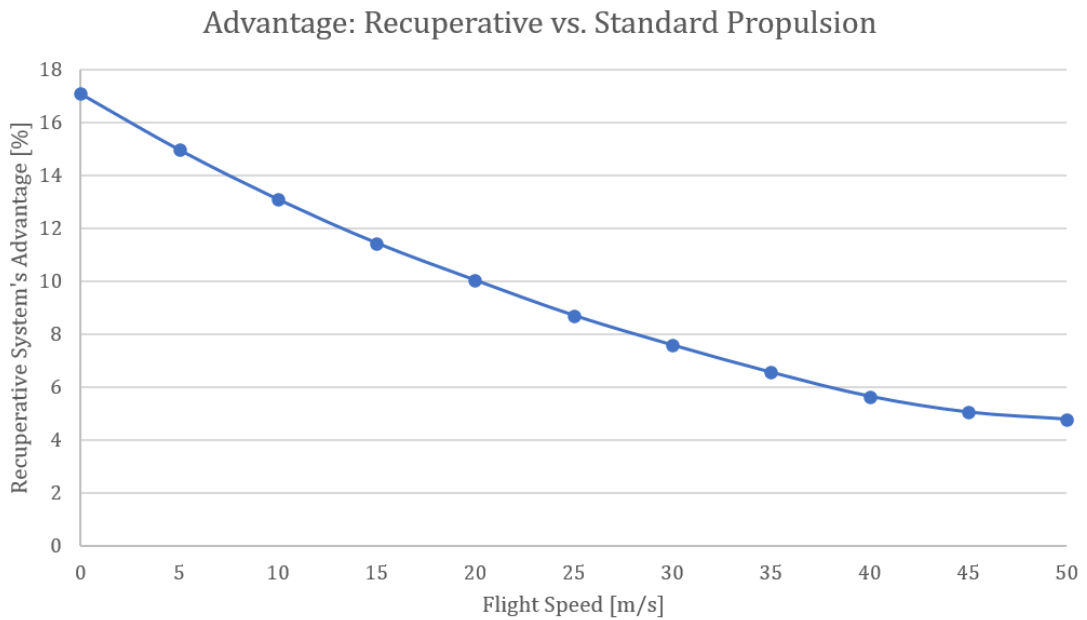
Figure 7.3: Advantage of Recuperative propulsion

7.2 A Few Notes on Comparison

Earlier in this thesis, in the theory chapter, the effect of nacelle drag was studied. Finally, the aerodynamic drag of the nacelle was evaluated in the first part of this chapter which compares the recuperative and standard propulsion systems. One of the attributes of the static recuperation propulsion is its possible installation *into* the fuselage and thereby eliminating the external nacelle drag. This phenomenon has not been evaluated in the CFD simulations. It would apparently even increase the recuperation system's advantage. Contrary, it is fair to say that the standard engine installation under the wings also brings some benefits. Namely it is improvement of wings' lift or, if designed appropriately, it helps to avoid flutter. Maintenance of an engine in an external nacelle is also much easier than of an engine built into the fuselage.

Also, there already are many aircraft designs that don't utilize external nacelle for their engines. Fighter jets typically have the engines mounted into the fuselage. This design has been also used for UL-39 Albi, an ultralight aircraft developed at CTU Prague. Another example is the first commercial jet airliner *de Havilland Comet* which had its engines mounted into the wing structure.

Chapter **8**

Conclusion

The aim of the present thesis was to examine the feasibility of the static recuperation aircraft propulsion system. First of all, in the introductory part, the history of aircraft propulsion was briefly described. After that, the most common aircraft propulsion systems were examined, including the theory behind them.

In the following chapter, the theory of recuperative propulsion was thoroughly studied. Four physical models with different degrees of fidelity were introduced in this chapter to illustrate the import of static recuperation. Based on the findings from the theoretical part, a concept of a propulsion system with static recuperation blades was designed. The additional thrust shall be generated on static blades situated in the wind flowing into the pressure sink in front of the electric motor-driven impeller.

Subsequently, a CFD analysis was performed for this model, using a 2D axisymmetric approximation. The results of this simulation have suggested that the model would need a refinement in order to work as intended. A few design changes had been made to the original model, which had a huge impact on its performance. The optimized model was then analyzed using the CFD simulation suchlike the original model. The data obtained by the simulation (the forces acting on the surfaces of interest) were thereafter studied, interpreted, and visualized. The results had shown, that the system can add almost 30 % of additive thrust relative to the primary source of thrust (the impeller). Even though the effect of the static recuperation decreased with increasing velocity, it still was able to produce some 10 % of additional thrust at flight speed equal to 30 m/s.

The original plan was to include real testing of a 3D printed model into this

thesis. This was planned to do in cooperation with company ZETJET AG, which gave me the opportunity to participate in their research of static recuperation. Unfortunately, universities were closed for most of 2020 due to the coronavirus pandemic, so the testing could not be done.

Future work

Aside from testing a real prototype of the propulsion system designed in this thesis, there is still room for improvement of the model by advanced CFD Simulation. In this thesis, an optimization was done mostly by trial and error and educated guesses. With more computational power, however, an algorithmic optimization could be done, by varying different parameters like blades inclination and position, shapes etc. Also, the impeller could be defined with higher fidelity, i.e. using real rotating blades. Another drawback of closed universities was that the simulations had to be done using an older personal laptop. It struggled to execute the CFD simulations and Fluent crashed on a regular basis.

Bibliography

[1] Mazyar Zeinali Daniel Rutherford. *Efficiency Trends for New Commercial Jet Aircraft 1960 to 2008*. 2009.

[2] Pratt & Whitney. *JT9D Fact Sheet*. accessed Oct 19, 2020. URL: `http://newsroom.prattwhitney.com/download/ce_jt9d_fact.pdf`.

[3] GE Aviation. *GEnx Fact Sheet*. accessed Oct 19, 2020. URL: `https://www.geaviation.com/commercial/engines/genx-engine`.

[4] Pratt & Whitney. *JT8D Fact Sheet*. accessed Oct 19, 2020. URL: `https://web.archive.org/web/20170510125602/http://pw.utc.com/Content/Press_Kits/pdf/me_jt8d-219_pCard.pdf`.

[5] EASA. *LEAP-1B EASA Type-Certificate*. accessed Oct 19, 2020. URL: `https://web.archive.org/web/20180404202036/https://www.easa.europa.eu/sites/default/files/dfu/EASA%20E115%20TCDS%20Issue%203%20LEAP-1B.pdf`.

[6] IATA. *Aircraft Technology Roadmap to 2050*. accessed Oct 20, 2020. URL: `https://www.iata.org/contentassets/8d19e716636a47c184e7221c77563c93/technology20roadmap20to20205020no20foreword.pdf`.

[7] KLM. *KLM and TU Delft present successful first flight Flying-V*. accessed Oct 21, 2020. URL: `https://news.klm.com/klm-and-tu-delft-present-successful-first-flight-flying-v/`.

[8] NASA. *NASA Armstrong Fact Sheet: X-48 Hybrid / Blended Wing Body*. accessed Oct 21, 2020. URL: `https://www.nasa.gov/centers/armstrong/news/FactSheets/FS-090-DFRC.html`.

[9] EU. *Clean Sky - SRIA Brochure intercalaires.* accessed Oct 21, 2020. URL: `http://clean-aviation.eu/files/Clean_Aviation_SRIA_16072020.pdf`.

[10] T. W. Lee. *Aerospace Propulsion.* John Wiley & Sons, Ltd, 2014.

[11] Gordon C. Oates. *Aerothermodynamics of Gas Turbine and Rocket Propulsion.* American Institute of Aeronautics and Astronautics, Inc., 1997.

[12] C. R. Peterson P. G. Hill. *Mechanics and thermodynamics of propulsion.* John Wiley & Sons, Ltd, 1992.

[13] Wikipedia. *Brayton cycle.* accessed Oct 22, 2020. URL: `https://en.wikipedia.org/wiki/Brayton_cycle`.

[14] Nicholas Cumpsty. *Jet propulsion.* Cambridge University Press, 2003.

[15] NASA. *The Evolution of Modern Aircraft.* accessed Oct 24, 2020. URL: `https://history.nasa.gov/SP-468/ch10-3.htm`.

[16] Safran. *LEAP 1-A Technical Characteristics.* accessed Oct 24, 2020. URL: `https://www.safran-aircraft-engines.com/commercial-engines/single-aisle-commercial-jets/leap/leap-1a`.

[17] Tomáš Vlach. *Design of a centrifugal compressor stage for a hybrid propulsion system.* Czech Technical University in Prague, 2020.

[18] Marek Janout. *Study of a Hybrid Propulsion System with Turbine Engine.* Czech Technical University in Prague, 2019.

[19] University of Illinois at Urbana-Champaign. *Putting hybrid-electric aircraft performance to the test.* accessed Oct 26, 2020. URL: `https://techxplore.com/news/2018-11-hybrid-electric-aircraft.html`.

[20] Saeed Farokhi. *Aircraft Propulsion.* John Wiley & Sons Ltd, 2014.

[21] Saeed Farokhi. *Future Propulsion Systems and Energy Sources in Sustainable Aviation.* John Wiley & Sons Ltd, 2020.

[22] Wenpig Cao. *Overview of Electric Motor Technologies Used for More Electric Aircraft.* IEEE (Institute of Electrical and Electronics Engineers), 2012.

[23] Siemens. *Siemens Electric Flight.* 2019. URL: `https://press.siemens.com/global/en/feature/electric-flight`.

[24] electricaltechnology.org. *Construction of a BLDC Motor*. accessed Dec 4, 2020. URL: https://www.electricaltechnology.org/wp-content/uploads/2016/05/Construction-of-a-BLDC-motor.jpg.

[25] A. M. Kuik V. L. Okulov J. N. Sorensen. *Development of the Optimum Rotor Theories*. Moscow-Izhevsk, 2013.

[26] Martin Ziegler. *Research Report, ZETJET-Aircraft Engines*. ZetJet AG, 2017.

[27] Michael Ivanovich. *Two New Metrics for Fan System Efficiency: Fan Energy Index and Fan Electrical Power*. Air Movement and Control Association (AMCA), 2017.

[28] David G. MacManus Matthew Robinson. *Aspects of aero-engine nacelle drag*. Journal of Aerospace Engineering, Cranfield University, Rolls-Royce, 2018.

[29] Martin Ziegler. *Gateway to All Electric Flight*. ZetJet AG, 2018.

[30] fanjetusa.com. *Fan Jet USA*. accessed Dec 23, 2020. URL: https://fanjetsusa.com/product/het-90mm-rotor-with-colet/.

[31] Airfoil Tools. *NACA 4 digit airfoil generator (NACA 9510 AIRFOIL)*. accessed Dec 23, 2020. URL: http://airfoiltools.com/airfoil/naca4digit?MNaca4DigitForm%5Bcamber%5D=9.4&MNaca4DigitForm%5Bposition%5D=50&MNaca4DigitForm%5Bthick%5D=10&MNaca4DigitForm%5BnumPoints%5D=81&MNaca4DigitForm%5BcosSpace%5D=0&MNaca4DigitForm%5BcosSpace%5D=1&MNaca4DigitForm%5BcloseTe%5D=0&yt0=Plot.

[32] Ansys. *Ansys Fluent 2020 R2 User's Guide*. accessed Jan 5, 2020. URL: https://ansyshelp.ansys.com/account/secured?returnurl=/Views/Secured/corp/v202/en/flu_ug/flu_ug_sec_compressible_when_to_use.html.

[33] Ansys. *Ansys Fluent 2020 R2 User's Guide*. accessed Dec 23, 2020. URL: https://ansyshelp.ansys.com/account/secured?returnurl=/Views/Secured/corp/v202/en/flu_ug/flu_ug_sdes_set.html?q=transient%20sst.

[34] Ansys. *Ansys Fluent 2020 R2 User's Guide*. accessed Dec 24, 2020. URL: https://ansyshelp.ansys.com/account/secured?returnurl=/Views/Secured/corp/v202/en/flu_ug/flu_ug_sec_graphics_pathlines.html?q=pathlines.

Appendices

Appendix A

Flow contours of the optimized model

A.1   Optimized model inlet velocity 0 m/s
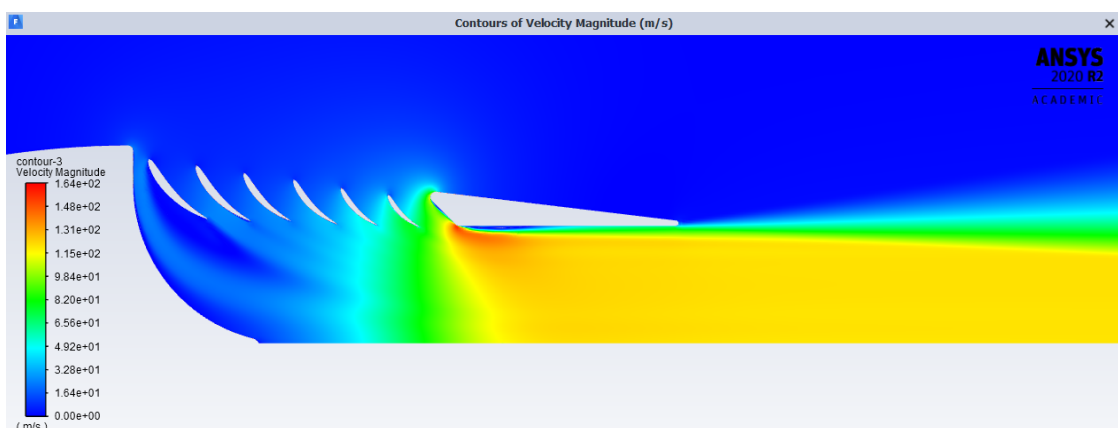
Figure A.1: Contours of the velocity magnitude for inlet velocity 0 m/s.
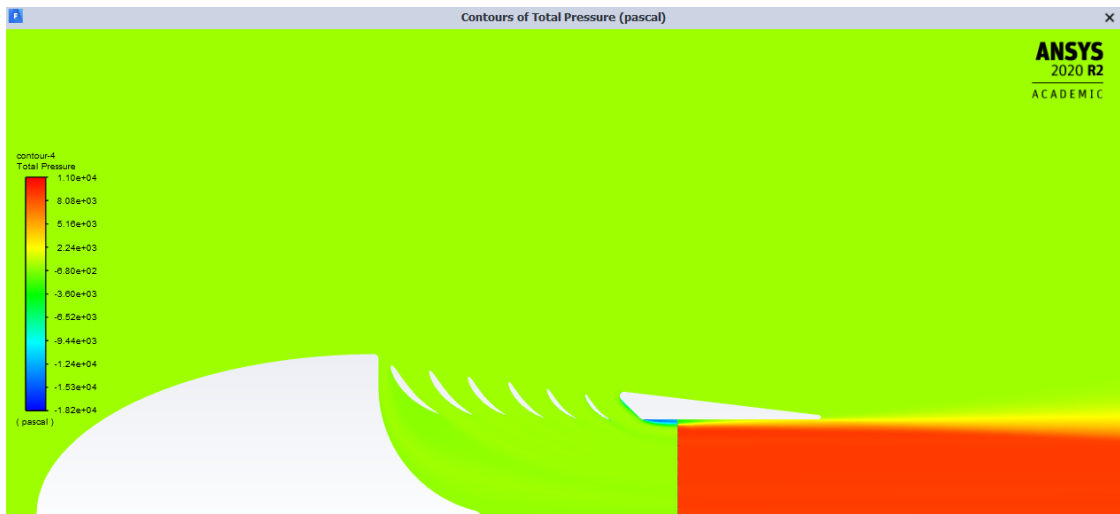
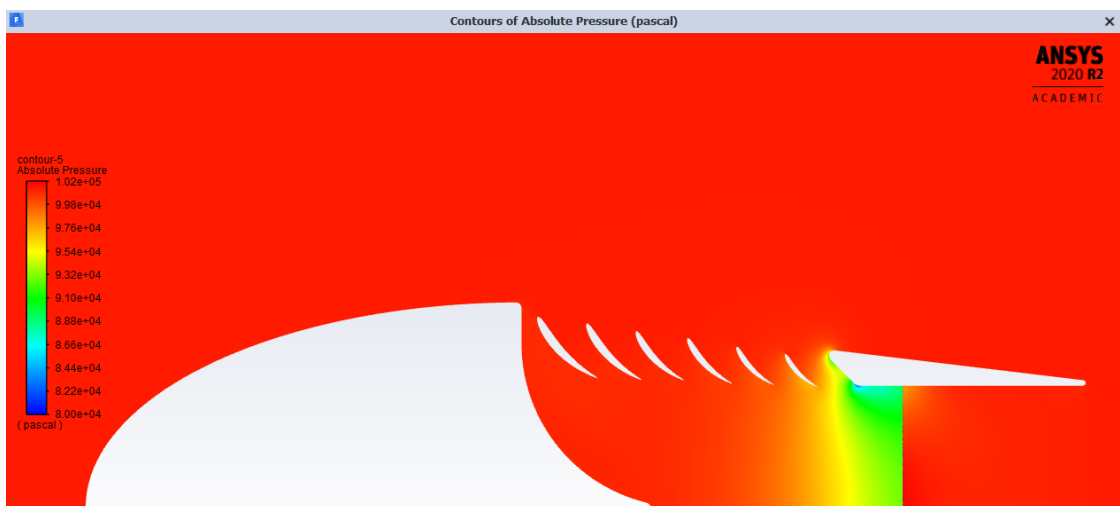**Figure A.2:** Contours of the total pressure for inlet velocity 0 m/s.

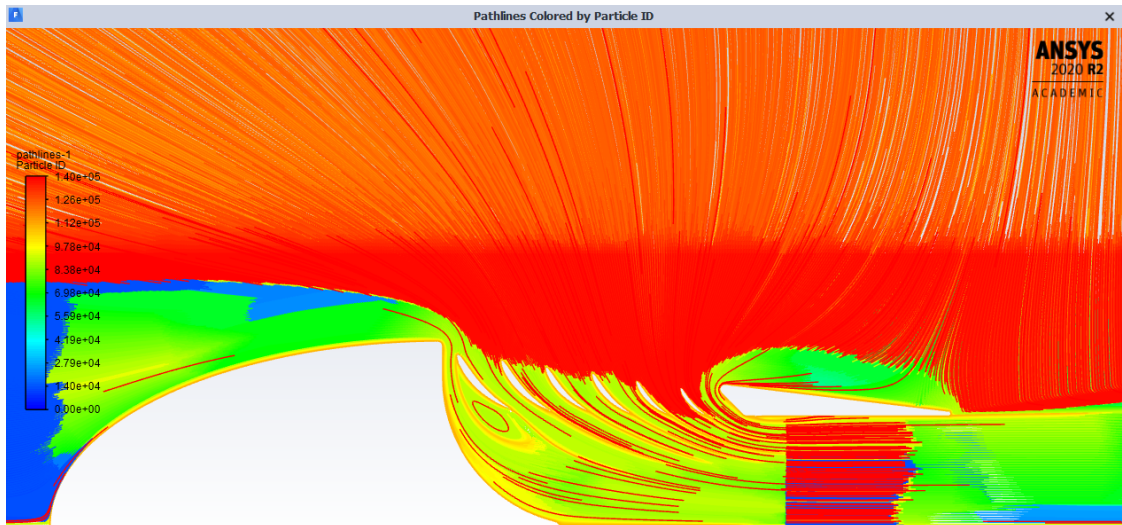**Figure A.3:** Contours of the absolute pressure for inlet velocity 0 m/s.

Figure A.4: Pathlines for inlet velocity 0 m/s.
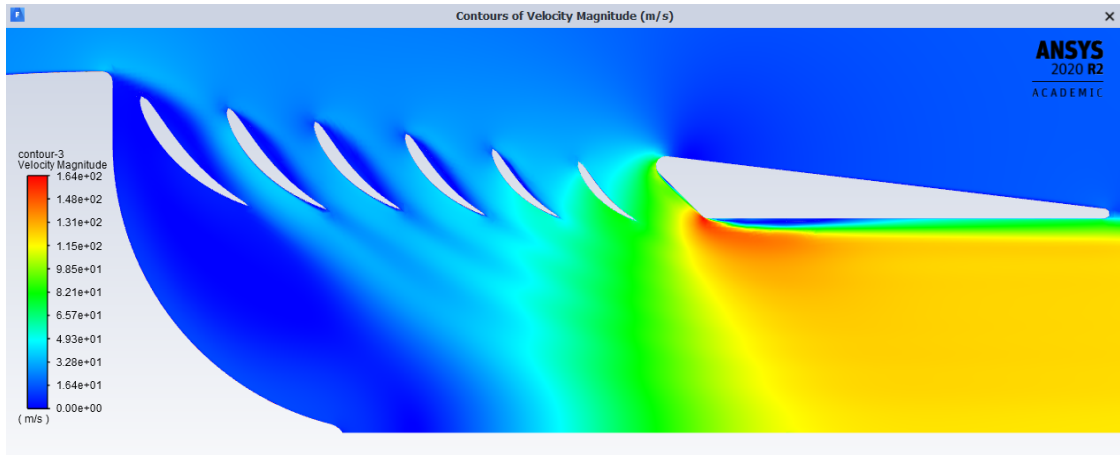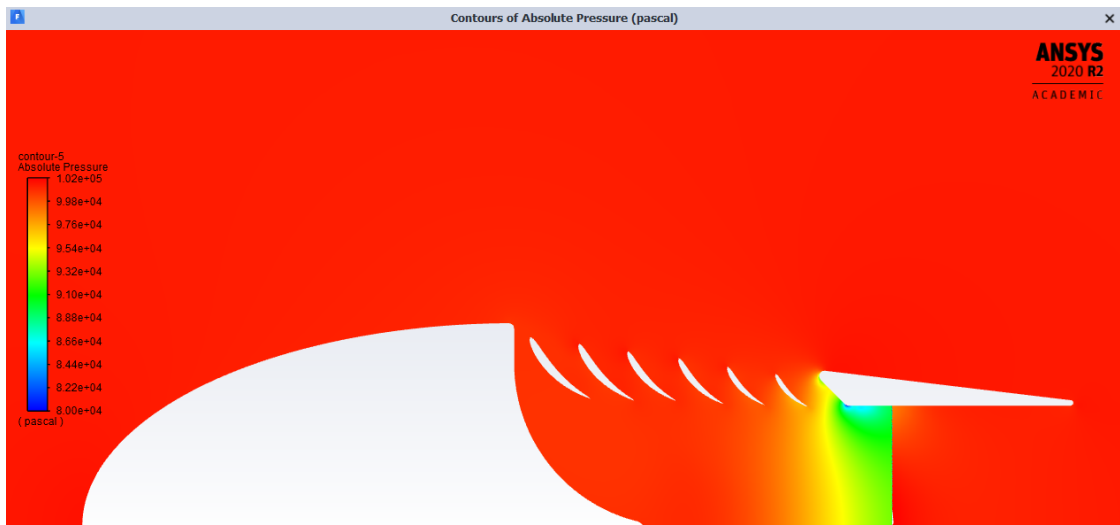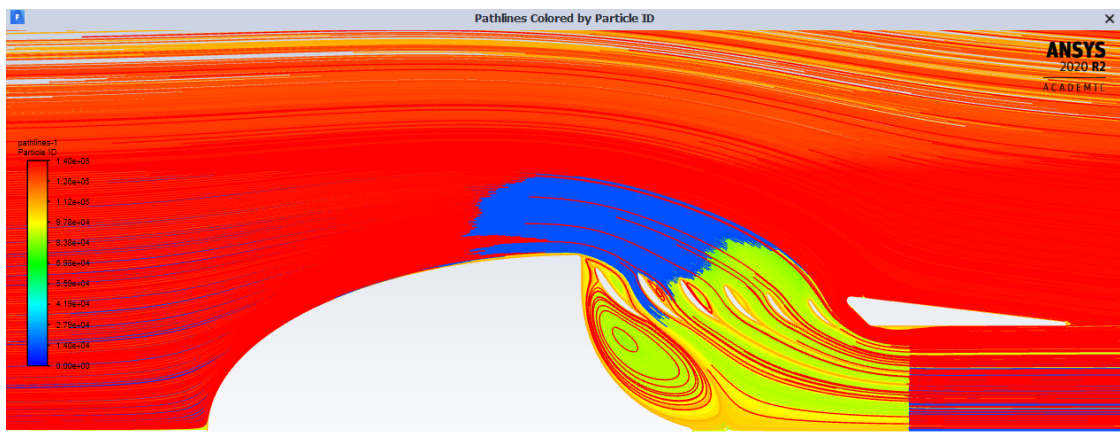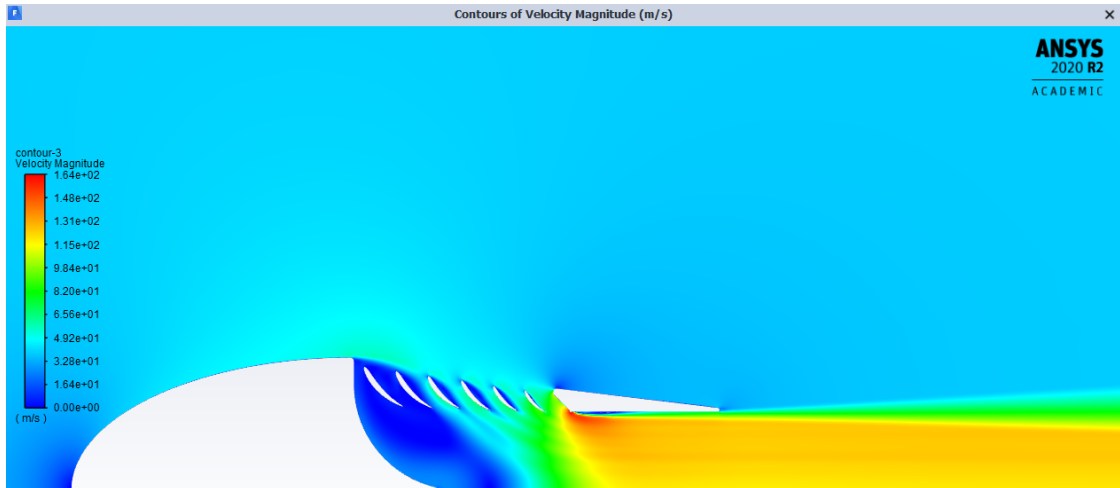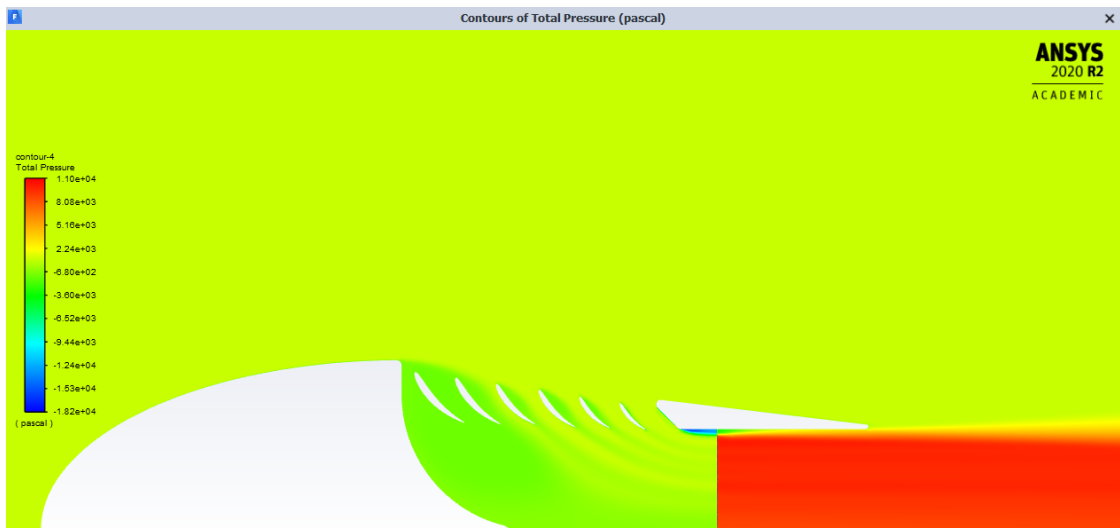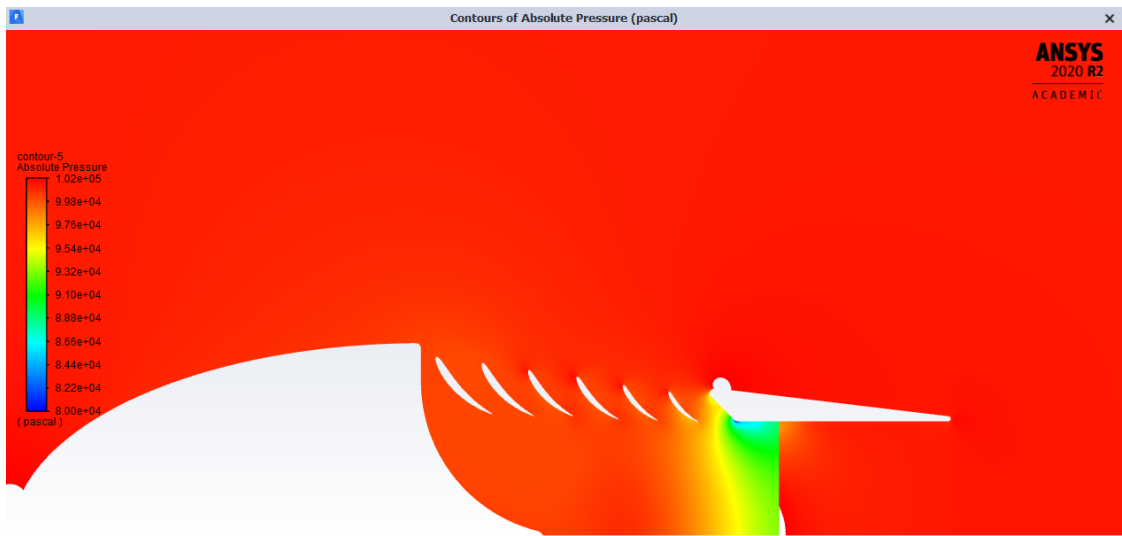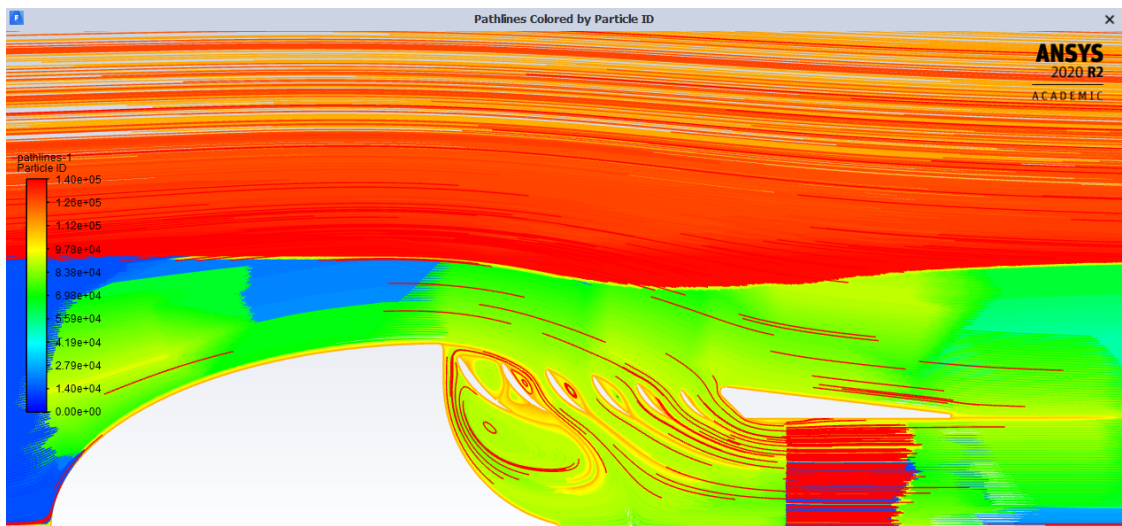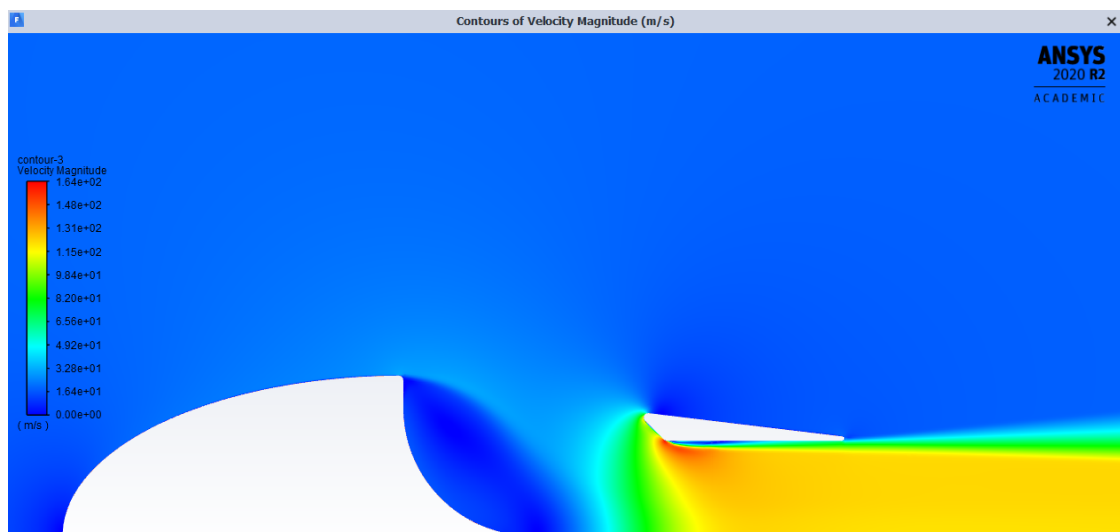
A.2 Optimized model inlet velocity 20 m/s

Figure A.5: Contours of the velocity magnitude for inlet velocity 20 m/s.

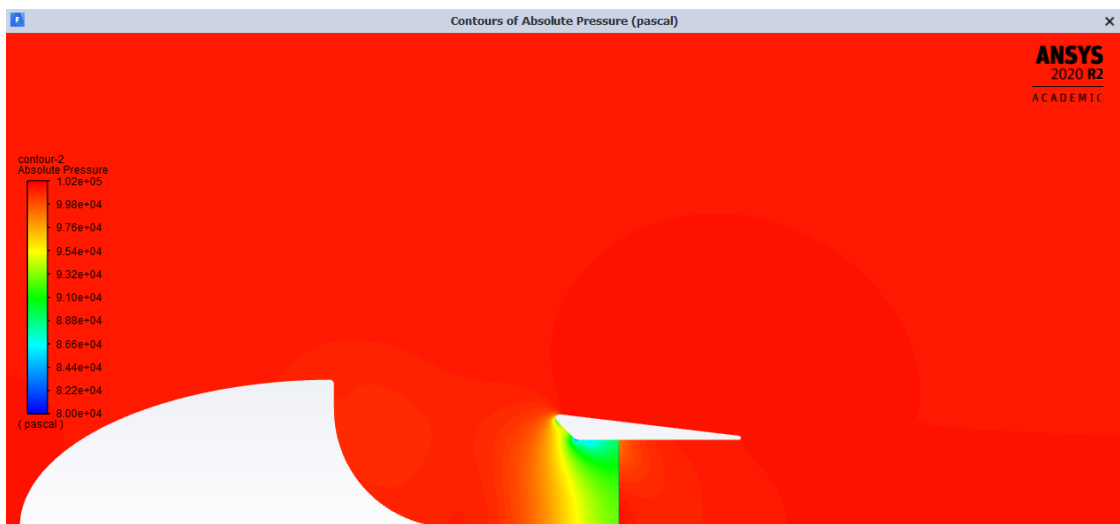**Figure A.6:** Contours of the total pressure for inlet velocity 20 m/s.

Figure A.7: Contours of the absolute pressure for inlet velocity 20 m/s.

Figure A.8: Pathlines for inlet velocity 20 m/s.

A.3   Optimized model inlet velocity 40 m/s

Figure A.9: Contours of the velocity magnitude for inlet velocity 40 m/s.

Figure A.10: Contours of the total pressure for inlet velocity 40 m/s.

83

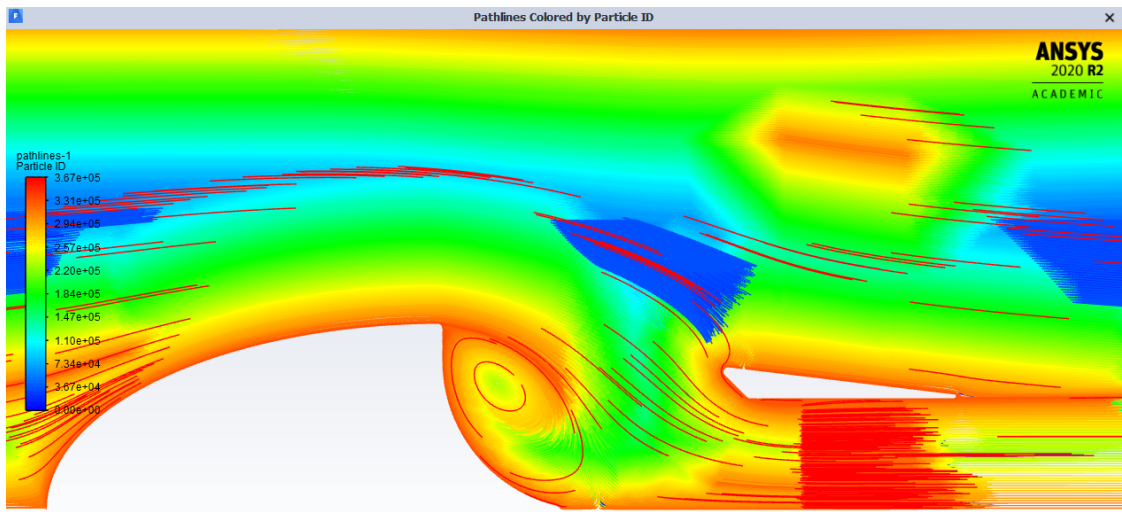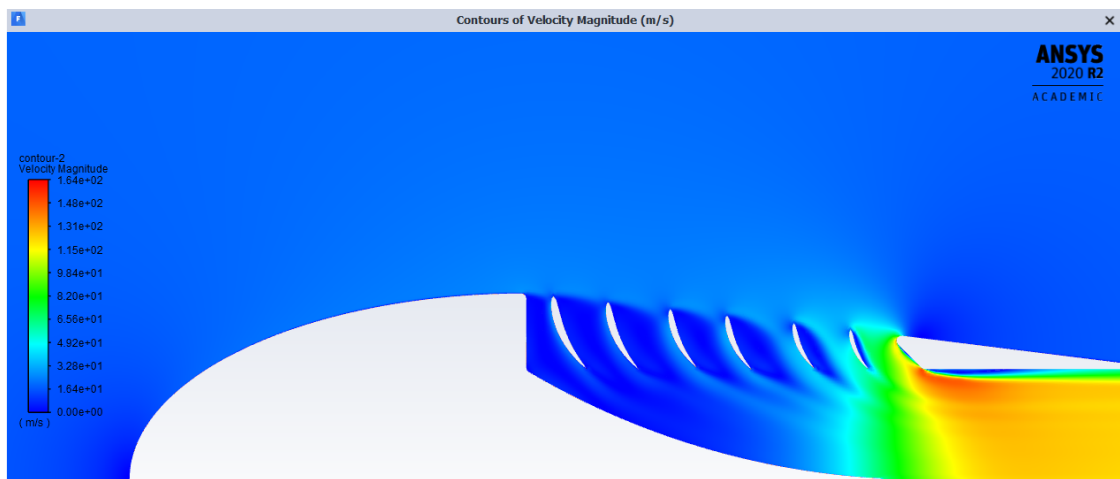**Figure A.11:** Contours of the absolute pressure for inlet velocity 40 m/s.

Figure A.12: Pathlines for inlet velocity 40 m/s.

Appendix B

Flow contours of the model without the blades

B.1   Model without the blades inlet velocity 20 m/s

Figure B.1: Contours of the velocity magnitude for inlet velocity 20 m/s.

Figure B.2: Contours of the total pressure for inlet velocity 20 m/s.

Figure B.3: Contours of the absolute pressure for inlet velocity 20 m/s.

Figure B.4: Pathlines for inlet velocity 20 m/s.

Appendix C

Flow contours of the original model

C.1   The original model inlet velocity 20 m/s

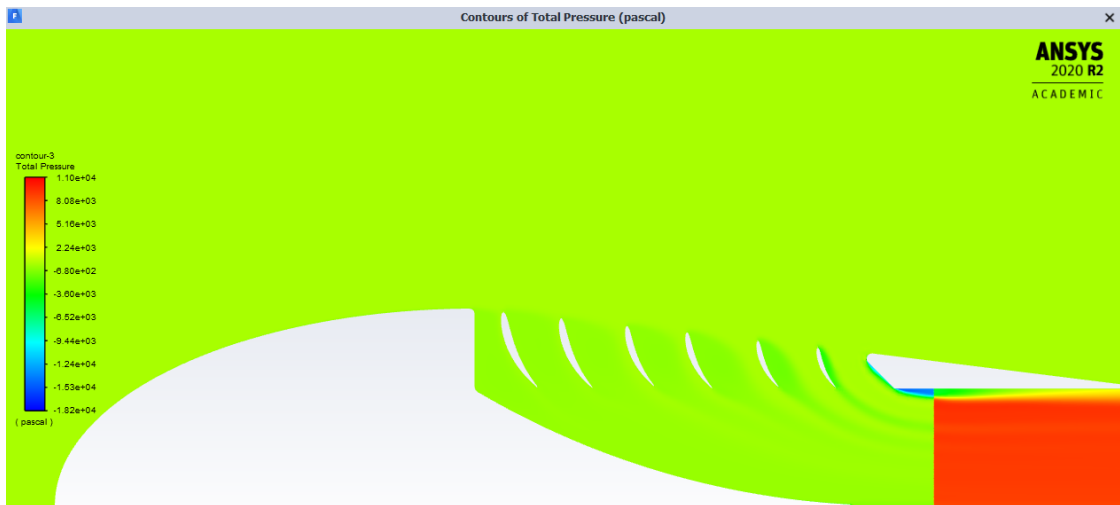**Figure C.1:** Contours of the velocity magnitude for inlet velocity 20 m/s.

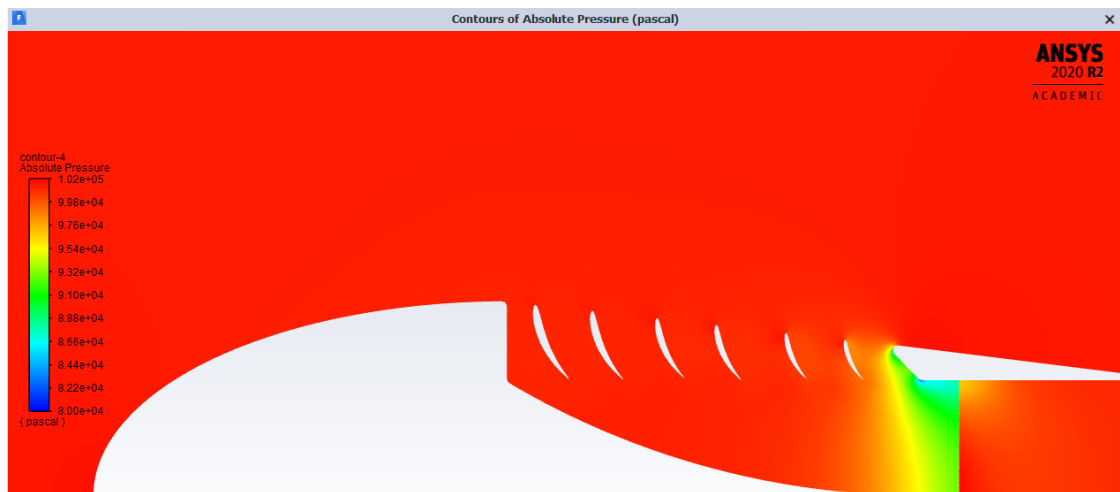**Figure C.2:** Contours of the total pressure for inlet velocity 20 m/s.
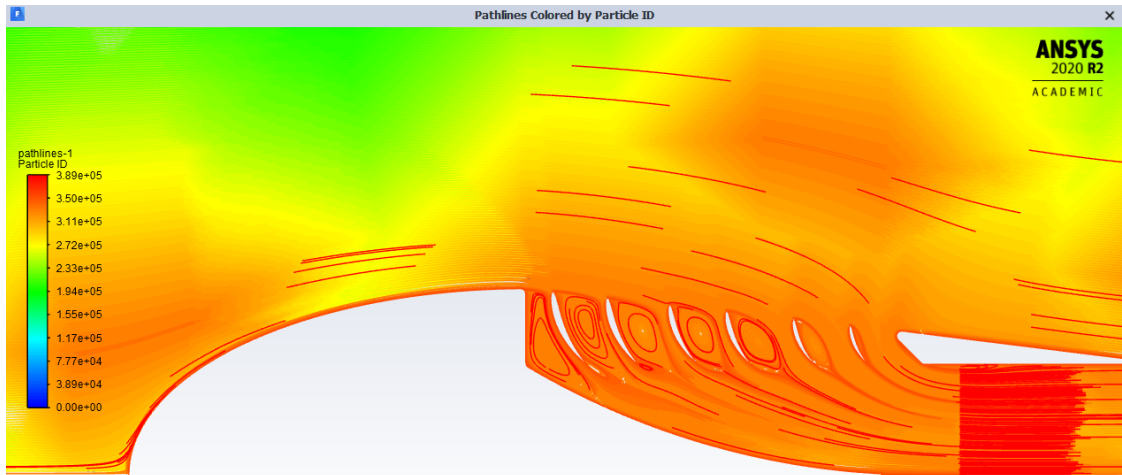

Figure C.3: Contours of the absolute pressure for inlet velocity 20 m/s.

Figure C.4: Pathlines for inlet velocity 20 m/s.